https://doi.org/10.5194/egusphere-2026-5035
Preprint. Discussion started: 18 September 2026

Initiation Timing Improves Retrogressive Thaw Slump Susceptibility Mapping on the Qinghai–Tibet Plateau

Pengfei Li[1,2], Zhuotong Nan[2*], Jiwei Xu[1], Fujun Niu[2]

[1]State Key Laboratory of Climate System Prediction and Risk Management, Nanjing Normal University, Nanjing, 210023, China
[2]Yangtze River Delta Urban Wetland Ecosystem National Field Scientific Observation and Research Station, School of Environmental and Geographical Sciences, Shanghai Normal University, Shanghai, 200234, China

[*] *Correspondence to*: Zhuotong Nan (nanzt@shnu.edu.cn)

Abstract. Accelerating retrogressive thaw slump (RTS) activity is reshaping permafrost landscapes on the Qinghai-Tibet Plateau (QTP) and threatening infrastructure. Forward-looking assessment requires identifying slopes approaching failure rather than mapping past RTS occurrence. Conventional susceptibility models treat RTS initiation as a binary outcome, making pre-initiation locations effectively equivalent regardless of when they subsequently fail. Yet under progressive environmental forcing, initiation timing can provide an implicit ordering of susceptibility: earlier initiation may indicate greater susceptibility than later initiation. We therefore defined Years Before Initiation (YBI) from annual inventories and developed a weakly supervised ranking framework that uses initiation-time ordering to learn susceptibility gradients. The Annual-YBI model was compared with two conventional models (Static Binary and Annual Binary) sharing the same neural network architecture. Although all models performed similarly in five-fold cross-validation (ROC-AUC ≈ 0.988), the Annual-YBI model captured 89.45% of 199 temporally held-out RTS initiations in 2021–2022 within the top 10% susceptibility area, compared with 79.90% and 63.82% for Annual Binary and Static Binary models, respectively. SHAP analysis identified NDVI, slope, and ground ice content as primary predisposing factors, with modulation by annual hydroclimatic variables. The 2021–2022 maximum susceptibility composite classified 1.70×10^5 km^2 (15.6% of QTP permafrost) as high or very high susceptibility, including 42.8% of permafrost within the 20-km Qinghai–Tibet Engineering Corridor buffer. These results show that initiation timing provides weak supervision for susceptibility gradients that binary labels cannot resolve, improving identification of locations prone to future RTS initiation and offering potential for transfer to other permafrost regions.

Keywords: Retrogressive thaw slump, Susceptibility mapping, Initiation timing, Weakly supervised learning, Qinghai–Tibet Plateau

https://doi.org/10.5194/egusphere-2026-5035
Preprint. Discussion started: 18 September 2026

1 Introduction

Retrogressive thaw slumps (RTSs) represent one of the most dynamic and rapidly evolving forms of permafrost degradation in ice-rich terrain. These slope failures occur when massive ground ice is exposed, triggering sustained headwall retreat, thaw consolidation, and downslope transport of saturated sediment (French, 2017; Kokelj and Jorgenson, 2013; Nesterova et al., 2024; Lewkowicz and Way, 2019). RTS activity can profoundly alter landscape evolution, carbon mobilization, water quality, and infrastructure stability (Luo et al., 2024; Ma et al., 2025). RTSs are observed across the circumpolar permafrost region, including the Arctic lowlands of Canada, Alaska, and Siberia, as well as high-mountain permafrost areas such as the Qinghai–Tibet Plateau (QTP) (Lewkowicz and Way, 2019; Makopoulou et al., 2024; Nesterova et al., 2024).

On the QTP, the largest and highest mid-latitude permafrost region on Earth, RTS activity has increased sharply over recent decades (Xia et al., 2024a). This rapid expansion coincides with accelerated permafrost warming and active-layer thickening across the plateau (Cheng and Wu, 2007; Ji et al., 2026). Similar increases in RTS activity and expansion have been documented in other permafrost regions under climate warming, including the Russian High Arctic and western Canadian Arctic (Barth et al., 2025; Segal et al., 2016). These changes highlight the need to identify locations where new RTSs are likely to initiate before visible failure occurs, particularly in regions where permafrost degradation intersects critical infrastructure.

Susceptibility mapping has become a widely used tool for identifying areas prone to future RTS initiation. Along the Qinghai–Tibet Engineering Corridor (QTEC), where critical transportation lifelines such as the Qinghai–Tibet Railway and Highway traverse highly warm and thermally unstable permafrost, proactive risk assessment is important for long-term infrastructure safety. For RTSs, however, susceptibility assessment presents a particular challenge because initiation is the outcome of progressive environmental change rather than a purely static spatial condition. Traditional approaches typically rely on static binary classification frameworks, in which multi-year RTS inventories are aggregated into a single "occurred versus not occurred" label and related to terrain, permafrost, vegetation, and climatic predictors using statistical or machine-learning models (Fan et al., 2025; He et al., 2024; Luo et al., 2024; Wang et al., 2024; Yin et al., 2021). These models have successfully identified important predisposing factors such as slope angle, ground ice content, and vegetation cover. However, by collapsing events observed over multiple years into a single binary occurrence label, they primarily learn where RTSs have occurred rather than how susceptibility may evolve before initiation. In particular, locations that have not yet failed are treated as the same class even though some may be approaching failure while others may remain substantially less susceptible. This formulation therefore treats RTS occurrence largely as a time-invariant spatial probability and overlooks the progressive, threshold-crossing nature of slope failure under long-term environmental forcing (Guzzetti et al., 2005, 2012; Reichenbach et al., 2018).

In response to the limitations of purely static susceptibility assessments (Zhu et al., 2026c), recent studies have increasingly developed dynamic susceptibility models that incorporate year-specific hydroclimatic variables (e.g., thawing degree days, soil moisture, and precipitation) to represent interannual variability in environmental conditions (Fan et al., 2025;

https://doi.org/10.5194/egusphere-2026-5035
Preprint. Discussion started: 18 September 2026

Zhu et al., 2026a). Such models better capture the role of changing environmental conditions in modulating permafrost slope stability. Nevertheless, their supervision generally remains binary: samples from the initiation year are treated as positive events, whereas locations without an observed initiation are treated as background or pseudo-absence. Thus, adding time-varying predictors does not by itself resolve the fundamental labeling problem: the models still lack information that distinguishes different degrees of pre-initiation susceptibility among locations that have not yet failed.

Annual RTS inventories contain an underused source of information that can help address this problem: the relative timing of initiation. Under progressive regional climate forcing, locations that initiate RTSs earlier may represent more susceptible environmental conditions than locations that initiate later. Importantly, this temporal ordering does not require direct observation of an unmeasurable "susceptibility state"; rather, the sequence of initiation events provides an indirect or weak supervision signal about relative susceptibility. The environmental states observed during the years preceding initiation can therefore provide information about a susceptibility gradient. Conventional binary formulations cannot exploit this ordering because they either discard pre-initiation observations or treat them simply as non-event background, thereby losing information about the progressive destabilization that precedes failure.

This distinction is also important in relation to process-based models of RTS evolution. Models such as RTSEvo (Xu et al., 2026) simulate the post-initiation growth and morphological development of existing RTSs and therefore provide valuable insight into how an established slump evolves. They do not, however, address the separate problem of identifying where new RTSs are likely to initiate.

To address this gap, we developed a weakly supervised ranking framework that uses the temporal order of RTS initiations to extract relative susceptibility information from annual inventories. Using the high-resolution annual inventory of Xia et al. (2024a), we defined Years Before Initiation (YBI) for RTS-related samples and integrated YBI-based pairwise ranking constraints within matched local spatiotemporal domains as an auxiliary supervision signal (Chaudhary et al., 2020). Rather than treating all pre-initiation samples as equivalent background, the framework constrains samples associated with earlier initiation to rank as more susceptible than those associated with later initiation. This enables the model to learn a more continuous susceptibility gradient leading toward RTS initiation while retaining the standard binary classification objective.

The objectives of this study are twofold: (1) to develop and evaluate a susceptibility mapping framework that incorporates the temporal order of RTS initiations, and (2) to determine whether this additional temporal-order information improves the identification of future RTS initiation relative to the Static Binary and Annual Binary approaches. We evaluate the three approaches using a common neural-network architecture, five-fold cross-validation, and independent temporal validation against temporally held-out RTS initiations in 2021 and 2022. By using initiation timing as weak supervision, we seek to bridge the gap between spatial pattern recognition and progressive pre-initiation evolution, thereby improving forward-looking RTS susceptibility assessment under ongoing climate warming on the QTP.

https://doi.org/10.5194/egusphere-2026-5035
Preprint. Discussion started: 18 September 2026

2 Study Area and Data

2.1 Study Area

The study area covers the permafrost region of the QTP, located between approximately 26°–40°N and 73°–105°E (Fig. 1). This region contains an estimated 1.086×10^6 km² of permafrost, accounting for approximately 41% of the plateau area and representing the largest and highest mid-latitude permafrost zone globally (Cao et al., 2023).With an average elevation exceeding 4,000 m, the QTP permafrost is characterized by relatively high ground temperatures, thin permafrost thickness, and low thermal stability, making it particularly vulnerable to climate warming and surface disturbances (Cheng and Wu, 2007; Zhao et al., 2020, 2021).

The permafrost region exhibits pronounced spatial heterogeneity in topography, ground ice conditions, vegetation cover, soil properties, and hydroclimatic conditions. Ground ice content generally increases from south to north and from east to west (Zou et al., 2024a), while climatic conditions follow a distinct southeast–northwest gradient. Mean annual air temperature ranges from −5.0 °C to 15.5 °C, and annual precipitation varies widely from 16 mm to 1,764 mm (Chen et al., 2015). Long-term borehole monitoring has documented continuous permafrost warming and progressive thickening of the active layer, indicating widespread permafrost degradation across the plateau (Zhao et al., 2020, 2021).

RTSs are widely distributed throughout the QTP permafrost domain, with particularly high concentrations in the central plateau where ground ice content is abundant (Xia et al., 2024b). In contrast, RTS activity tends to be more localized along the eastern and western margins, where topographic and hydrological conditions exert stronger control. The recent availability of high-resolution annual inventories from 2016 to 2022 makes the QTP well suited to testing how initiation timing can be incorporated into susceptibility mapping.

https://doi.org/10.5194/egusphere-2026-5035
Preprint. Discussion started: 18 September 2026

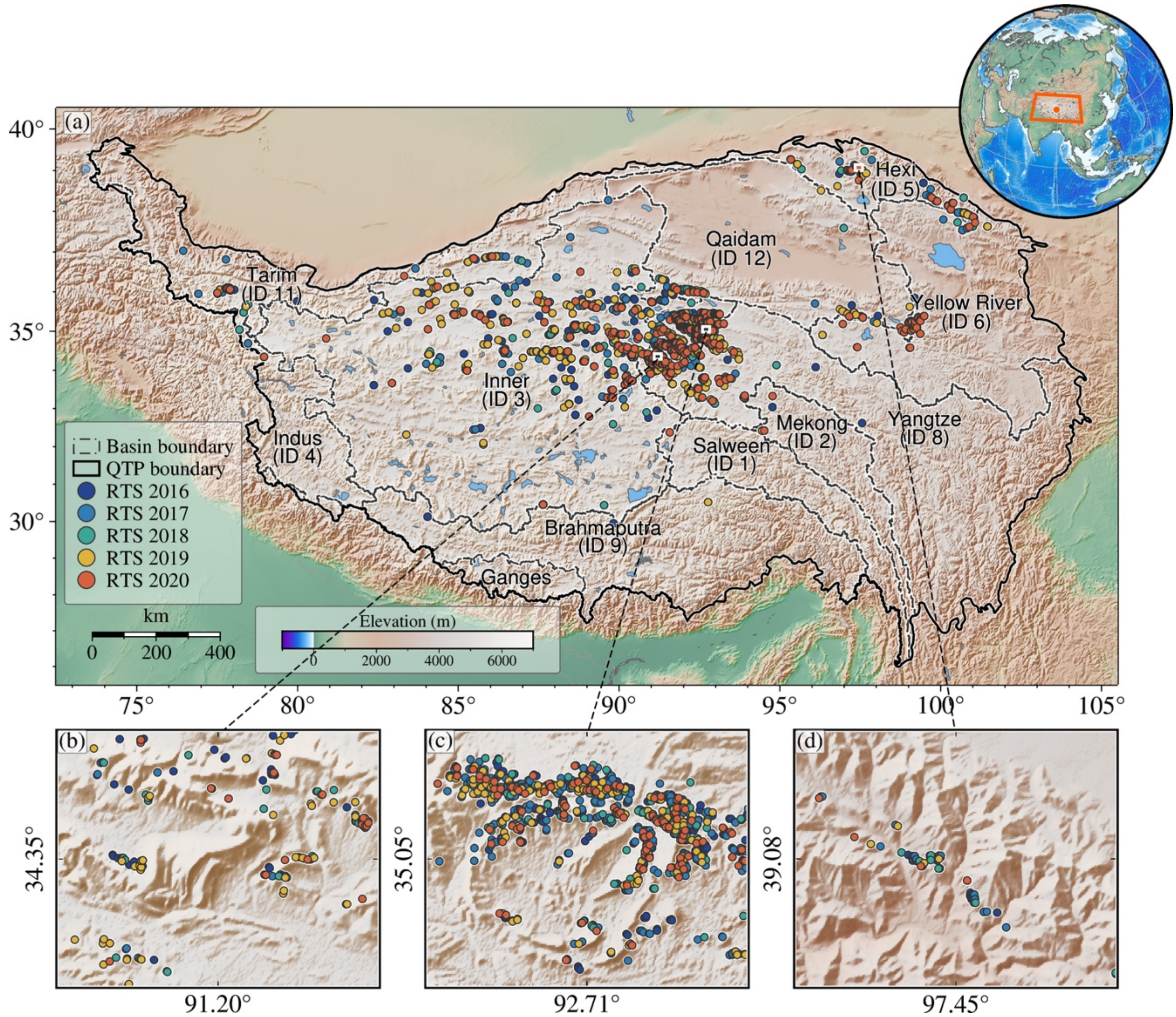

Fig. 1 Location of the study area and spatial distribution of retrogressive thaw slumps (RTSs) on the Qinghai–Tibet Plateau (QTP). (a) Distribution of RTSs within the permafrost region from 2016 to 2020. Colored dots represent the year of first detection (blue = 2016; red = 2020). Background shading indicates elevation. (b–d) Enlarged views of representative RTS clusters showing local spatial distribution patterns.

2.2 Annual RTS Inventory

This study uses the high-resolution annual RTS inventory developed by Xia et al. (2024a) for the QTP. The inventory was generated using multitemporal PlanetScope imagery (3–5 m spatial resolution) combined with a deep learning-assisted mapping workflow and subsequent manual verification. It provides annual delineations of active RTS features from 2016 to 2022 across the entire permafrost region of the QTP.

According to the inventory, the number of active RTS sites increased from 1,592 in 2016 to 3,805 in 2022, while the total affected area expanded from 1,714 ha to 6,507 ha. Each RTS polygon has an associated year of first detection, which is used here as a proxy for initiation year, enabling the reconstruction of temporal dynamics.

https://doi.org/10.5194/egusphere-2026-5035
Preprint. Discussion started: 18 September 2026

Unlike conventional susceptibility studies that use initiation year solely as a binary occurrence label, this study treats initiation timing as an additional source of information on slope susceptibility. Under ongoing climate forcing, slopes that initiate earlier have, on average, crossed the failure threshold sooner than slopes that initiate later. Consequently, environmental conditions observed before initiation may contain information about a slope's proximity to failure.

To exploit this information, two categories of RTS-related samples were extracted from each RTS polygon: (a) Initiation-year samples were extracted from the year when an RTS was first detected. These are treated as positive samples in the binary classification task and assigned the highest rank in the ordering framework. (b) Pre-initiation samples were extracted from the same RTS locations in the 1–4 years prior to initiation. Although no visible RTS feature was mapped during these years, these records capture environmental conditions preceding mapped initiation. Each sample was assigned a Years Before Initiation (YBI) value ranging from 1 to 4, and the relative ordering of these values was used as a weak supervision signal.

In addition, background pseudo-absence samples were randomly generated across the QTP region at locations where no RTS activity was observed at any time during the entire 2016–2022 period. To minimize potential label contamination, all pseudo-absence samples were required to be located at least 1,000 m from any mapped RTS polygon.

This sampling strategy allows the construction of both a binary classification dataset and a temporally ordered YBI ranking dataset. The latter forms the foundation of the proposed weakly supervised ranking framework, allowing temporal information contained in the annual inventory to be incorporated directly into susceptibility modeling.

2.3 Environmental Predictors

A total of 14 environmental predictors were selected to characterize the conditions associated with RTS initiation. These variables were grouped into four categories: terrain attributes, soil and permafrost properties, vegetation and surface ecological conditions, and hydroclimatic forcing (Table 1; Supplementary Fig. S1). The distributions of these predictors for RTS samples are shown in Supplementary Fig. S2. Predictor selection was guided by the current understanding of RTS development and its controlling factors reported in previous studies (Luo et al., 2024; Xia et al., 2024b; Yin et al., 2021). To assess potential multicollinearity, variance inflation factors were calculated for all predictors, and all values were below the commonly accepted threshold of 7 (Supplementary Fig. S3).

Terrain attributes represent the topographic controls on slope instability and surface water redistribution. Four variables were considered: slope, aspect, topographic wetness index (TWI), and local relief. These variables were derived from the SRTM V4 digital elevation model at 90 m resolution (Jarvis et al., 2008). Slope and local relief influence gravitational potential and sediment transport capacity, whereas aspect affects incoming solar radiation and ground thermal conditions. TWI was included as a proxy for the potential accumulation of soil moisture and surface runoff (Lehner et al., 2008).

Soil and permafrost properties describe the material characteristics governing thaw settlement and ground-ice degradation. Two variables were included: soil fine fraction and ground ice content (GIC). Soil fine fraction (clay and silt content) was extracted from SoilGrids 2.0 at 250 m resolution and calculated as a thickness-weighted average over the upper 0–200 cm profile (Poggio et al., 2021). GIC was obtained from the dataset Permafrost Ground-Ice Content to 10 m Depth on the Qinghai-Tibet Plateau at 1 km resolution (Zou et al., 2024a). Together, these variables represent the susceptibility of frozen ground to thaw-induced deformation and slope failure.

Vegetation and ecological surface conditions are represented by vegetation type and normalized difference vegetation index (NDVI). Vegetation type was derived from the TP_LC10-2022 land cover product at 10 m resolution (Huang et al., 2023). Warm-season NDVI was calculated from MODIS MOD13Q1 imagery at 250 m resolution (Didan, 2021). Vegetation influences permafrost stability through multiple mechanisms, including surface shading, evapotranspiration, insulation effects, and root reinforcement.

Hydroclimatic forcing variables were included to capture the thermal and hydrological conditions that influence RTS initiation at interannual timescales. Six dynamic variables were considered: thawing degree days (TDD), summer maximum daily precipitation (SMDP), annual precipitation, warm-season maximum temperature (WSTmax), warm-season relative humidity (WSRH), and summer soil moisture. Climate variables were derived from the ERA5-Land reanalysis dataset at 11.1 km resolution (Muñoz-Sabater et al., 2021), whereas soil moisture was obtained from the enhanced SMAP products at 9 km resolution (Entekhabi et al., 2010). These variables represent key thermal and hydrological conditions affecting active-layer thaw, ground moisture conditions, and the likelihood of RTS initiation.

Table 1 Environmental predictors, data sources, spatial resolution, and variable type.

Category	Variable	Data source	Resolution	Type
Terrain	Slope	CGIAR-SRTM V4 (Jarvis et al., 2008)	90 m	Static
	Aspect	CGIAR-SRTM V4 (Jarvis et al., 2008)	90 m	Categorical
	Topographic Wetness Index (TWI)	SRTM / HydroSHEDS (Lehner et al., 2008)	90 m	Static
	Local relief	CGIAR-SRTM V4 (Jarvis et al., 2008)	90 m	Static
Soil / permafrost	Soil fine fraction	SoilGrids 2.0 (Poggio et al., 2021)	250 m	Static
	Ground Ice Content (GIC)	Permafrost ground-ice content to 10 m depth on the Qinghai-Tibet Plateau (Zou et al., 2024b)	1 km	Static
Vegetation	Vegetation type	TP_LC10-2022 (Huang et al., 2023)	10 m	Categorical
	Normalized Difference Vegetation Index (NDVI)	MODIS MOD13Q1 (Didan, 2021)	250 m	Dynamic
Hydroclimate	Thawing Degree Days (TDD)	ERA5-Land (Muñoz Sabater, 2019)	11.1 km	Dynamic
	Summer Maximum Daily Precipitation (SMDP)	ERA5-Land (Muñoz Sabater, 2019)	11.1 km	Dynamic
	Annual Precipitation	ERA5-Land (Muñoz Sabater,	11.1 km	Dynamic

https://doi.org/10.5194/egusphere-2026-5035
Preprint. Discussion started: 18 September 2026

	2019)		
Warm-Season Maximum Temperature (WSTmax)	ERA5-Land (Muñoz Sabater, 2019)	11.1 km	Dynamic
Warm-Season Relative Humidity (WSRH)	ERA5-Land (Muñoz Sabater, 2019)	11.1 km	Dynamic
Summer Soil Moisture	SMAP enhanced (O'Neill et al., 2023)	9 km	Dynamic

2.4 Data Preprocessing and Spatiotemporal Sample Construction

All environmental data layers were projected and resampled to a unified 100-m Albers equal-area grid to ensure spatial consistency across datasets. Static predictors were assigned to each grid cell and remained constant across years, whereas dynamic hydroclimatic predictors were extracted according to the corresponding year of observation. Continuous variables were standardized using the mean and standard deviation calculated from the 2016–2020 training samples, and the same parameters were applied to validation folds and prediction grids to avoid data leakage. Vegetation type was converted using a one-hot encoding, with missing values treated as an additional category. Missing values in continuous predictors were imputed using the median values computed from the corresponding training fold.

Based on the preprocessed predictors and the sample definitions in Section 2.2, two complementary datasets were constructed for model development. The first is a binary dataset, which includes only initiation-year RTS samples and matched background pseudo-absence samples (7,672 positive and 7,672 negative samples; total n = 15,344). This dataset is used for standard binary susceptibility modeling. The second is the YBI ranking dataset, which extends the binary dataset by including 11,042 pre-initiation samples, yielding a total of 26,386 samples. In the YBI dataset, each sample is assigned a rank that reflects its temporal proximity to RTS initiation. For illustration, consider the observation year of 2016. This year contributes a spatial sequence of samples with varying temporal proximities to their respective initiation years: a polygon initiating in 2016 (YBI = 0, Rank = 5), a polygon initiating in 2017 (YBI = 1, Rank = 4), a polygon initiating in 2018 (YBI = 2, Rank = 3), a polygon initiating in 2019 (YBI = 3, Rank = 2), and a polygon initiating in 2020 (YBI = 4, Rank = 1). Together, these ranks define an ordered sequence from the earlies pre-initiation stage (Rank =1) to the highest expected susceptibility state at initiation (Rank = 5) within the observation year. The spatiotemporal sample construction workflow of the proposed framework, illustrating the generation of the two complementary datasets (the binary dataset and the YBI ranking dataset) across the environmental observation years (t), is schematically depicted in Fig. 2.

Within each local spatial cluster, the model is trained to learn this monotonic relationship by assigning progressively higher susceptibility scores as samples approach the initiation year. Background pseudo-absence samples are assigned to Rank = 0 and serve as reference anchors representing the lowest expected susceptibility state within the ordering space. They are not interpreted as truly nonsusceptible terrain, but as spatial anchors defining the lower bound of the susceptibility–ordering space. This relative ordering structure is later used as an auxiliary supervision signal during model training (see Section 3.2), enabling the model to learn a continuous susceptibility gradient rather than a strictly binary separation.

https://doi.org/10.5194/egusphere-2026-5035
Preprint. Discussion started: 18 September 2026

The detailed sample composition is summarized in Table 2. The spatial organization of samples across DBSCAN-derived clusters and hydrological basins is illustrated in Supplementary Fig. S4.

Table 2 Sample composition and supervision semantics of the binary and years-before-initiation (YBI) ranking datasets.

Dataset	Sample type	YBI	Binary Label (y)	Rank (r)	Count
Binary dataset	Background pseudo-absence	–	0	–	7,672
Binary dataset	Initiation-year RTS	0	1	–	7,672
YBI ranking dataset	Background pseudo-absence	–	0	0	7,672
YBI ranking dataset	Pre-initiation RTS record	1–4	–	1–4	11,042
YBI ranking dataset	Initiation-year RTS	0	1	5	7,672

Note: – indicates not applicable; numerical ranges (e.g., 1–4) indicate the corresponding range of YBI or rank values. Higher rank values indicate greater relative susceptibility, with Rank = 5 assigned to initiation-year samples.

https://doi.org/10.5194/egusphere-2026-5035
Preprint. Discussion started: 18 September 2026

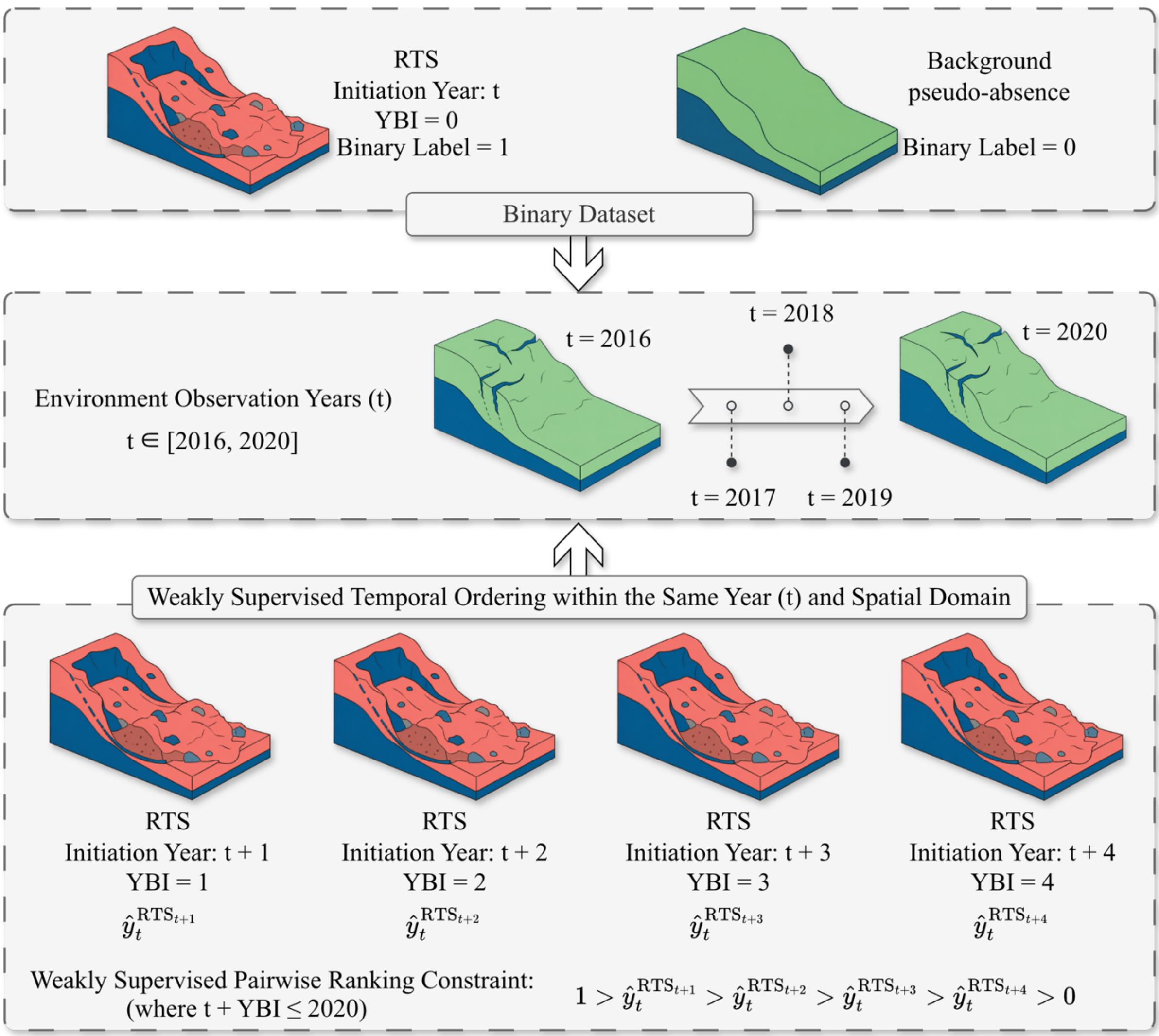

Fig. 2 Spatiotemporal sample construction workflow of the proposed framework, illustrating the generation of two complementary datasets (the binary dataset and the YBI ranking dataset). The binary dataset uses annual RTS initiation-year samples (YBI = 0) and a matched number of background pseudo-absence samples generated for each observation year *t*. The YBI ranking dataset extends the binary dataset by incorporating pre-initiation samples through a weakly supervised temporal ordering strategy. For each environmental observation year *t*, the environmental states of slopes that will initiate in subsequent years (t + YBI) are extracted in year *t* and defined as pre-initiation samples, subject to the temporal boundary condition of t + YBI <= 2020 (corresponding to YBI ∈ $[1, 2020 - t]$). Pairwise ranking constraints (i.e., $1 > \hat{y}_t^{\mathrm{RTS}_{t+1}} > \hat{y}_t^{\mathrm{RTS}_{t+2}} > \hat{y}_t^{\mathrm{RTS}_{t+3}} > \hat{y}_t^{\mathrm{RTS}_{t+4}} > 0$) are enforced within the same observation year and local spatial comparability domain to guide the model in learning a progressive, pre-initiation susceptibility gradient.

https://doi.org/10.5194/egusphere-2026-5035
Preprint. Discussion started: 18 September 2026

3 Methods

3.1 Modeling Strategies and Neural Network Architecture

To evaluate the effectiveness of the proposed YBI-based weakly supervised ranking framework, we compare three modeling strategies that share an identical neural network architecture but differ in their treatment of temporal information:

1) Model 1 (Static Binary): A baseline model that uses temporally aggregated (multi-year averaged) environmental predictors and treats all RTS samples as static binary labels (occurrence vs. pseudo-absence).

2) Model 2 (Annual Binary): A binary classification model that uses year-specific environmental predictors but does not include pre-initiation samples or ranking constraints.

3) Model 3 (Annual-YBI): The proposed model, which uses the same year-specific predictors as Model 2, but further incorporates pre-initiation samples through YBI-based pairwise ranking constraints.

All three models adopt an identical multi-layer perceptron (MLP) architecture to ensure a controlled and fair comparison. The network consists of three hidden layers with 128, 64, and 32 neurons, respectively. Rectified linear unit (ReLU) activation is applied after each hidden layer, followed by batch normalization and dropout (rate = 0.2) to reduce overfitting. The final output layer produces a single scalar value, which is passed through a sigmoid activation function to generate a continuous susceptibility score ranging from 0 to 1.

Using the same architecture helps ensure that performance differences among the three models reflects the modeling strategy (static, annual, or ranking-enhanced) rather than differences in network capacity or complexity.

3.2 Joint Loss Function

The proposed model (Model 3) is trained using a joint loss function that combines a primary binary classification objective with an auxiliary ranking regularization term:

$$\mathcal{L} = \mathcal{L}_{\mathrm{BCE}} + \lambda \mathcal{L}_{\mathrm{Rank}} \tag{1}$$

where $\mathcal{L}_{\mathrm{BCE}}$ denotes the masked binary cross-entropy loss, $\mathcal{L}_{\mathrm{Rank}}$ denotes the LambdaRank pairwise ranking loss, and λ is a hyperparameter that controls the strength of the ranking constraints.

The binary classification loss is computed only on samples with explicit supervision labels (i.e., initiation-year samples and background pseudo-absence samples). Pre-initiation samples are excluded from this loss term. It is defined as:

$$\mathcal{L}_{\mathrm{BCE}} = -\frac{1}{\mathrm{N}} \sum_{i=1}^{N} m_i \left[y_i \log(\hat{y}_i) + (1 - y_i) \log(1 - \hat{y}_i) \right] \tag{2}$$

where $y_i \in \{0,1\}$ is the binary label, $\hat{y}_i$ is the predicted susceptibility score, m_i is a binary mask equal to 1 for labeled samples and 0 for pre-initiation samples, and N is the batch size.

The ranking loss is the key component that encodes temporal ordering information. For any valid pair of samples (i, j) within the same local spatial domain, if sample i has a smaller YBI value than sample j (i.e., i is temporally closer to initiation),

https://doi.org/10.5194/egusphere-2026-5035
Preprint. Discussion started: 18 September 2026

the model is encouraged to assign a higher susceptibility score to i than to j ($\hat{y}_i > \hat{y}_j$). This is implemented using the LambdaRank formulation:

$$\mathcal{L}_{\text{Rank}} = \frac{1}{\sum_{(i,j)\in\mathcal{P}} w_{ij}} \sum_{(i,j)\in\mathcal{P}} w_{ij} \log\left(1 + \exp\left[-\sigma\left(\hat{y}_{i_i} - \hat{y}_j\right)\right]\right) \tag{3}$$

where $\mathcal{P}$ denotes the set of valid ranking pairs, σ is a scaling factor, and w_{ij} represents the change in Normalized Discounted Cumulative Gain (NDCG) resulting from swapping the positions of samples i and j (Burges et al., 2007).

The hyperparameter λ was tuned through grid search on the validation set within the range [0,1], and the value yielding the best cross-validation performance was selected for final model training.

3.3 Spatial Comparability Domains and Ranking Constraints

To construct meaningful ranking pairs, we evaluated three spatial comparability domains:

1) Global domain: All samples from the same year across the entire QTP are considered comparable.

2) Basin domain: Samples are only compared within the same hydrological basin and within the same year.

3) DBSCAN domain: Samples are only compared within local spatial clusters identified by Density-Based Spatial Clustering of Applications with Noise (DBSCAN) using eps = 50 km and min_samples = 5. The clustering parameters were selected to capture regional-scale RTS aggregation patterns while avoiding overly fragmented or overly generalized spatial groupings.

In cross-validation, the DBSCAN domain achieved the best overall performance. This likely reflects the strong spatial clustering of RTS activity and the greater comparability of topographic, permafrost, and climatic conditions within local clusters than across global or basin-scale domains. The spatial grouping schemes are illustrated in Fig. 3. Accordingly, comparing their temporal order (YBI) within these local domains is more physically meaningful.

Within each DBSCAN cluster and within the same year, pairwise ranking constraints are generated as follows: (a) Any two pre-initiation samples, or a pre-initiation sample and an initiation-year sample, can form a valid pair. (b) If sample i has a smaller YBI value than sample j (i.e., i is temporally closer to initiation), the model is constrained to assign a higher susceptibility score to i than to j; (c) Background pseudo-absence samples are assigned Rank = 0 and are paired with all RTS-related samples within the same cluster. This local pairwise ranking mechanism forms the core of the weakly supervised temporal ordering framework. It enables the model to learn a continuous susceptibility gradient that respects the inventory-derived temporal ordering of RTS initiations, rather than treating all positive samples as homogeneous. In this framework, YBI represents the inventory-derived temporal distance to initiation, while the ranking variable (Rank) is a monotonic transformation used to encode this temporal information into an ordered supervision structure. The LambdaRank loss then operates on pairwise comparisons derived from this ordering, enabling the model to learn relative susceptibility rather than absolute temporal values.

https://doi.org/10.5194/egusphere-2026-5035
Preprint. Discussion started: 18 September 2026

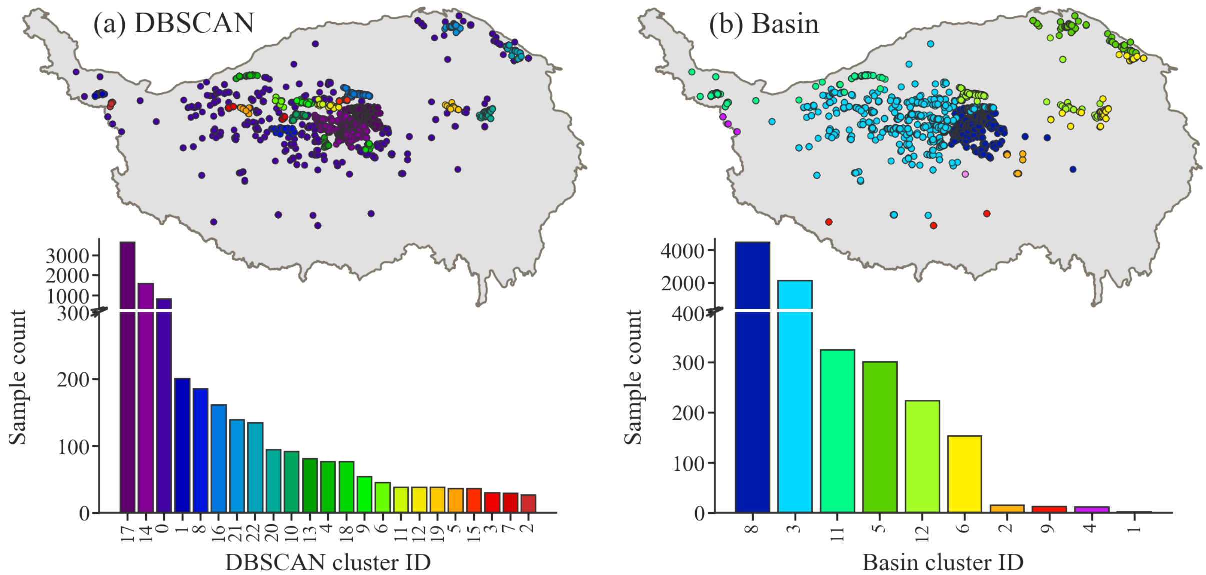

Fig. 3 Spatial distribution of RTS samples and sample counts across different spatial grouping schemes. (a) DBSCAN cluster distribution (top) and corresponding sample counts per cluster (bottom). (b) Basin cluster distribution (top) and corresponding sample counts per cluster (bottom). Only major clusters with sufficient sample sizes are labeled on the x-axis for clarity.

3.4 Training Procedure and Hyperparameter Optimization

All models were trained using five-fold stratified group cross-validation to prevent data leakage. Because multiple annual samples can originate from the same RTS polygon, the RTS polygon ID was used as the grouping key. This ensures that all samples belonging to the same RTS are assigned entirely to either the training or validation fold, preventing records from the same RTS from being split across folds and reducing within-event spatial and temporal dependence.

Within each training fold, two key hyperparameters were optimized through sensitivity analysis: the ranking loss weight λ (searched over the range [0, 1]) and the batch size. $\lambda = 0.4$ was selected as it yielded the best overall results across all six evaluation metrics (Supplementary Fig. S5). A batch size of 256 was chosen as it provided stable performance (Supplementary Fig. S6). All other hyperparameters (learning rate = 0.001, dropout rate = 0.2) were kept identical across the three models to ensure a controlled and fair comparison.

Training was performed using the Adam optimizer with early stopping based on validation loss (patience = 15 epochs). The model with the lowest validation loss was retained for final evaluation. All experiments were implemented in PyTorch, with a fixed random seed used to ensure reproducibility.

3.5 Independent Temporal Validation and Uncertainty Quantification

To assess forward generalization, we performed independent temporal validation using future initiations held out from model fitting. Specifically, all models were trained exclusively on 2016–2020 samples, while new RTS initiations from 2021

https://doi.org/10.5194/egusphere-2026-5035
Preprint. Discussion started: 18 September 2026

(n = 174) and 2022 (n = 25) were reserved as an independent temporal validation set. This design provides a temporally held-out evaluation of forward generalization by excluding 2021–2022 RTS initiation samples from model fitting.

Given the strong spatial imbalance of RTS occurrences, percentile-based evaluation was used to directly assess the ability of the model to concentrate new RTS initiations within the high-susceptibility tail of the predicted distribution, thereby evaluating spatial concentration without relying on a fixed classification threshold. For each new RTS initiation, we extracted its predicted susceptibility score from the corresponding annual susceptibility map and computed its percentile rank within the full study area. We then calculated the proportion of validation points falling into the top 10%, 20%, and 30% susceptibility zones. Higher capture rates in the high-susceptibility tail indicate better predictive skill.

In addition, we quantified spatial prediction uncertainty using the five-fold ensemble. For each grid cell, the final susceptibility score was computed as the mean prediction across the five ensemble members, while uncertainty was quantified by the standard deviation across the five ensemble members. The continuous uncertainty values were classified into five levels using the Jenks natural breaks method (Jenks, 1967) to facilitate spatial visualization and interpretation. By combining the mean susceptibility level and the uncertainty level, we generated a two-dimensional susceptibility-uncertainty map. Since both susceptibility and uncertainty were classified into five levels, this resulted in 25 possible combined categories (e.g., high susceptibility with low uncertainty representing relatively robust high-susceptibility zones). This map classifies each grid cell into one of 25 combined categories, allowing identification of relatively robust high-susceptibility zones (high susceptibility with low uncertainty) as well as areas requiring further investigation (high susceptibility with high uncertainty).

3.6 Model Interpretation Using SHAP

To interpret the trained Annual-YBI model (Model 3) and quantify the contribution of individual predictors, we employed SHAP (SHapley Additive exPlanations) values (Lundberg and Lee, 2017). SHAP values were computed for the ensemble of five cross-validation models using their respective out-of-fold validation samples from 2016 to 2020, based on the model-agnostic Permutation Explainer algorithm implemented in the SHAP Python package. Global feature importance was calculated as the mean absolute SHAP value across all samples. Beeswarm plots were generated to visualize both the magnitude and direction of each predictor's influence, while SHAP dependence plots were used to illustrate the marginal association of individual predictors with susceptibility.

4 Results

4.1 Cross-Validation Performance

All three models were assessed via five-fold stratified group cross-validation with RTS polygon ID as the grouping key to prevent data leakage. Performance was evaluated within the DBSCAN spatial domain. All models exhibited consistently high and stable classification performance (Table 3). Model 3 (Annual-YBI) achieved a ROC-AUC = 0.988 ± 0.001, precision = 0.928 ± 0.009, recall = 0.970 ± 0.004, F1-score = 0.949 ± 0.003, and Kappa = 0.895 ± 0.007, which were very similar to

https://doi.org/10.5194/egusphere-2026-5035
Preprint. Discussion started: 18 September 2026

those of Model 2 (Annual Binary). Model 3 showed marginally higher accuracy (0.948 ± 0.003) and F1-score than Model 2. Model 1 (Static Binary) exhibited slightly higher scores overall, although differences among the three models were small (< 0.01 in most metrics).

Training converged within 30–50 epochs with low inter-fold variability (Fig. 4a). Averaged confusion matrices (Fig. 4b) indicate well-balanced precision and recall, with miss rates of approximately 3% and false alarm rates of approximately 7% across all models.

These results indicate that the YBI ranking constraints can be incorporated into the learning framework without degrading the primary binary classification performance. Predictive performance for future RTS initiations is further evaluated in the independent temporal validation section below.

Table 3 Five-fold cross-validation performance of the three modeling strategies. Values are reported as mean ± standard deviation across the five folds.

Model	ROC-AUC	Accuracy	Precision	Recall	F1 score	Kappa
Model 1 (Static Binary)	0.988±0.001	0.951±0.003	0.933±0.006	0.971±0.005	0.952±0.003	0.902±0.005
Model 2 (Annual Binary)	0.988±0.001	0.947±0.004	0.928±0.008	0.969±0.003	0.948±0.003	0.894±0.007
Model 3 (Annual-YBI)	0.988±0.001	0.948±0.003	0.928±0.009	0.970±0.004	0.949±0.003	0.895±0.007

https://doi.org/10.5194/egusphere-2026-5035
Preprint. Discussion started: 18 September 2026

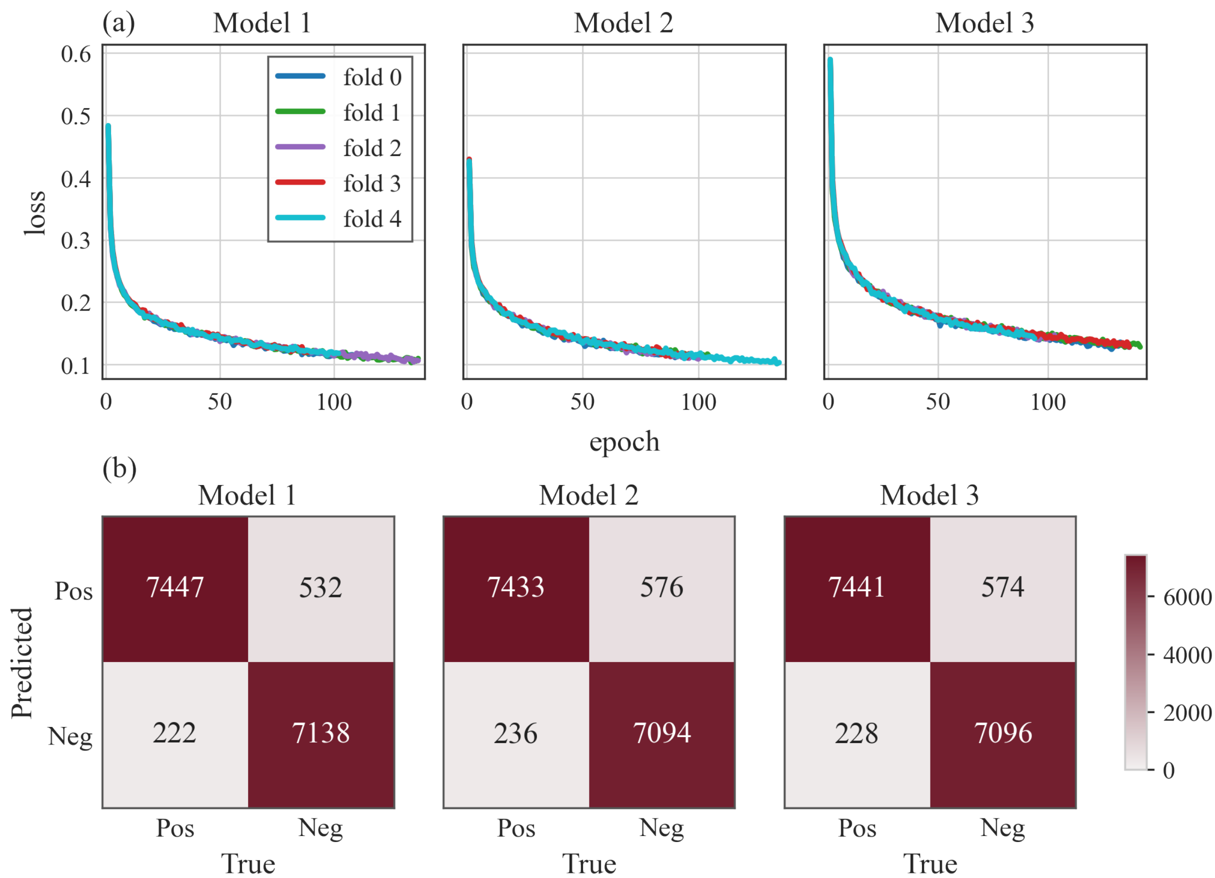

Fig. 4 Training dynamics and classification performance of the three models. (a) Training loss curves across five cross-validation folds. (b) Confusion matrices averaged across five folds for Model 1, Model 2, and Model 3.

4.2 Independent Temporal Validation

To evaluate the models' ability to predict future RTS initiations, all three models were trained exclusively on 2016–2020 data and evaluated against temporally held-out RTS initiations recorded in 2021 (n = 174) and 2022 (n = 25).

Independent temporal validation revealed clear differences in predictive performance among the three models (Fig. 5). The Annual-YBI model (Model 3) placed 89.45% of the 199 temporally held-out RTS initiation points in the top 10% of the susceptibility distribution, compared with 79.90% for the Annual Binary model (Model 2) and 63.82% for the Static Binary model (Model 1). The median percentile ranks of the validation points were 97.46% (Model 3), 96.27% (Model 2), and 93.88% (Model 1). Corresponding median predicted susceptibility scores were 0.874 (Model 3), 0.729 (Model 2), and 0.533 (Model 1).

When validation points was summarized by susceptibility intervals, Model 3 captured 76.88% (153/199) of the new RTS points in the high or very high classes (≥ 0.6), versus 63.32% for Model 2 and 48.24% for Model 1 (Fig. 6). The proportion of validation points falling into the very low susceptibility class (< 0.2) decreased from 32.66% under Model 1 to 9.55% under

https://doi.org/10.5194/egusphere-2026-5035
Preprint. Discussion started: 18 September 2026

Model 3. These results demonstrate that the YBI ranking constraints improved the capture of future RTS initiations while only modestly expanding the high-susceptibility area and without degrading cross-validation performance. The consistent
355 improvement across multiple metrics indicates a systematic rightward shift of future RTS locations toward higher susceptibility values, rather than improvement driven by a small number of individual cases.

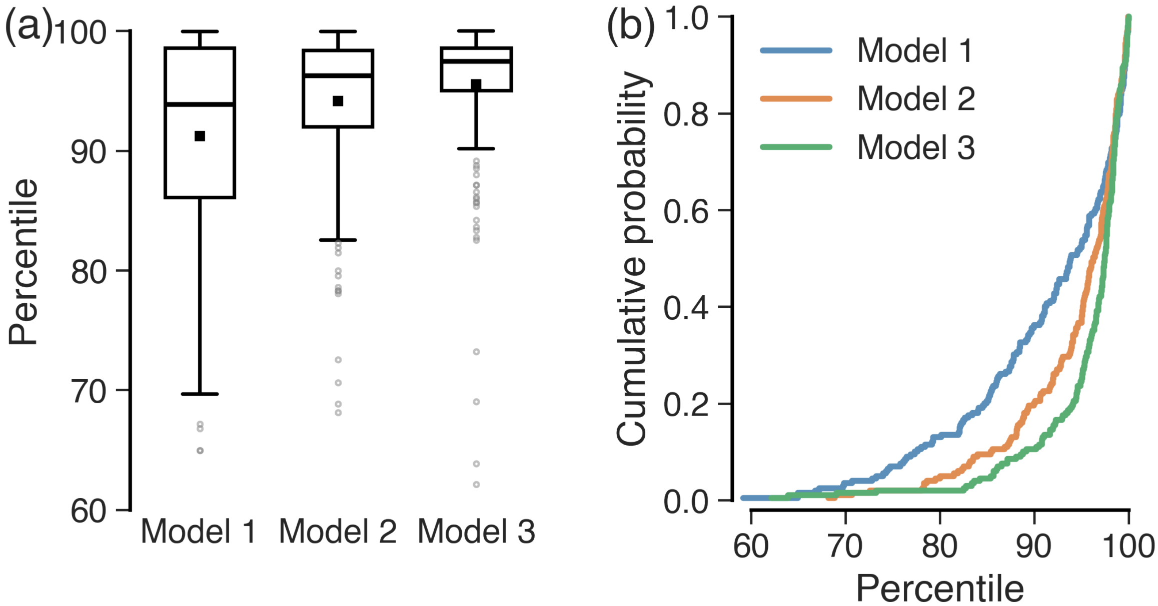

Fig. 5 Percentile ranks and empirical cumulative distribution function (ECDF) curves of independent temporal validation locations on the susceptibility maps. (a) Boxplots of percentile ranks for the 2021 cohort (n = 174) and 2022 cohort (n = 25). (b) ECDF curves
360 **showing how strongly each model concentrates validation locations in the upper susceptibility percentiles.**

https://doi.org/10.5194/egusphere-2026-5035
Preprint. Discussion started: 18 September 2026

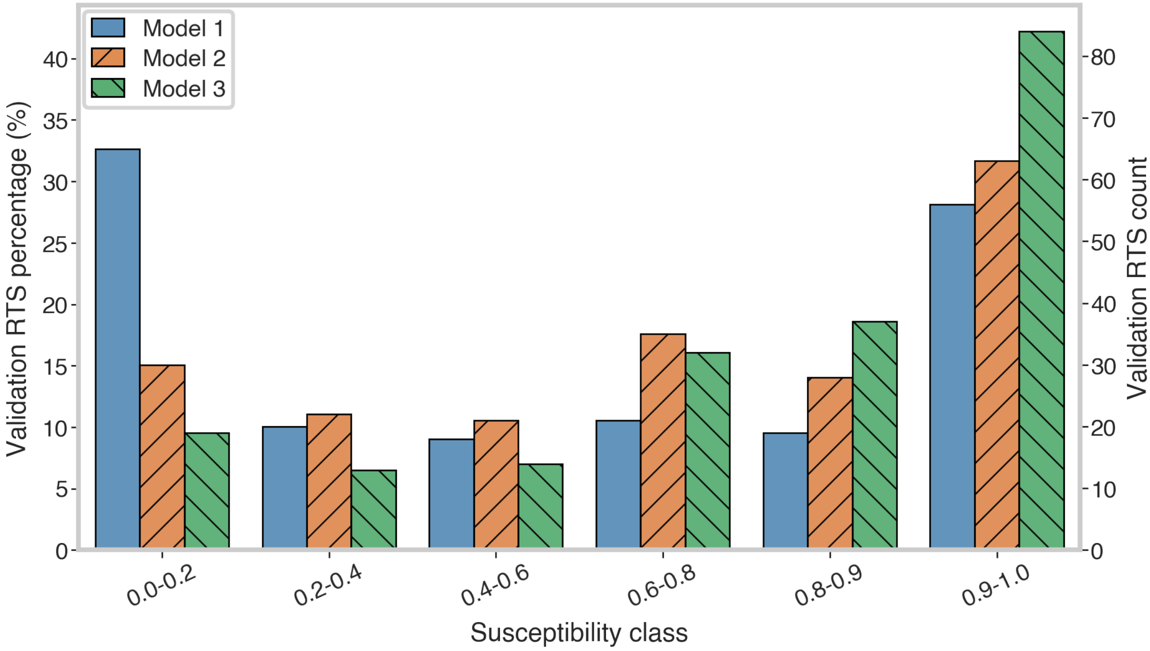

Fig. 6 Distribution of the 199 independent temporal validation RTS points (2021–2022) across six susceptibility intervals for the three models.

4.3 RTS Susceptibility Mapping and Spatial Uncertainty

The susceptibility maps produced by the three models showed broadly consistent spatial patterns, with high-susceptibility zones concentrated in the central permafrost region of the QTP (Supplementary Figs. S7–S8). At broad spatial scales, the three models produced similar patterns, although minor differences in the fine-scale pattern and connectivity of high-susceptibility patches were visible in the enlarged subregions. Across the study area, more than 91.5% of the permafrost region was classified as low or very low susceptibility (< 0.4) by all models. The extent of the very high susceptibility class (0.8–1.0) varied only modestly among models and remained stable between years (Supplementary Fig. S9).

Uncertainty in the susceptibility predictions was quantified as the standard deviation of predictions from the five cross-validation folds of Model 3. Fig. 7 presents the ensemble mean susceptibility and corresponding prediction uncertainty for 2021 and 2022. Model 3 exhibited high spatial consistency across the permafrost region. The mean standard deviation was low in both years (0.0229 in 2021 and 0.0267 in 2022). In 2021, 81.36% of the area was classified as very low uncertainty (standard deviation ≤ 0.0261), while only 1.90% fell into the very high uncertainty category (standard deviation > 0.2242). In 2022, overall uncertainty increased slightly, with 79.76% in the very low uncertainty class and 2.30% in the very high uncertainty class. The combined high and very high uncertainty area increased from 5.55% in 2021 to 6.37% in 2022, mainly in topographically complex transition zones.

https://doi.org/10.5194/egusphere-2026-5035
Preprint. Discussion started: 18 September 2026

At the pixel level, mean susceptibility and prediction uncertainty showed a moderate positive spatial correlation (r = 0.5725 in 2021 and r = 0.5901 in 2022). The very high susceptibility class exhibited approximately five times higher uncertainty (mean standard deviation = 0.0468–0.0507) than the very low susceptibility class (0.0088–0.0099). Low-susceptibility areas showed greater agreement among ensemble members, whereas high-susceptibility areas, often associated with more complex terrain and nonlinear interactions, showed greater inter-fold variability. Importantly, even in high-susceptibility zones, the absolute uncertainty (standard deviation ≈ 0.05) remained much smaller than the spacing between susceptibility classes (0.10–0.20), suggesting that ensemble variability was generally modest relative to the susceptibility-class intervals.

To provide decision-relevant reliability information, a bivariate classification of five susceptibility levels and five uncertainty levels was performed, resulting in 25 combined categories (Supplementary Fig. S10). Four key reliability types were identified: (1) high-susceptibility with low uncertainty (relatively robust high-susceptibility zones, representing priority areas for field investigation and monitoring), (2) high-susceptibility with high uncertainty (priority targets for field investigation and validation; these areas were mainly located in geological and climatic transition zones and complex valley systems with strong local heterogeneity), (3) low-susceptibility with low uncertainty (low-susceptibility background areas), and (4) low-susceptibility with high uncertainty (areas with low predicted susceptibility but higher sensitivity to training perturbations, warranting further examination). This uncertainty-aware classification distinguishes relatively robust predictions from areas requiring additional verification.

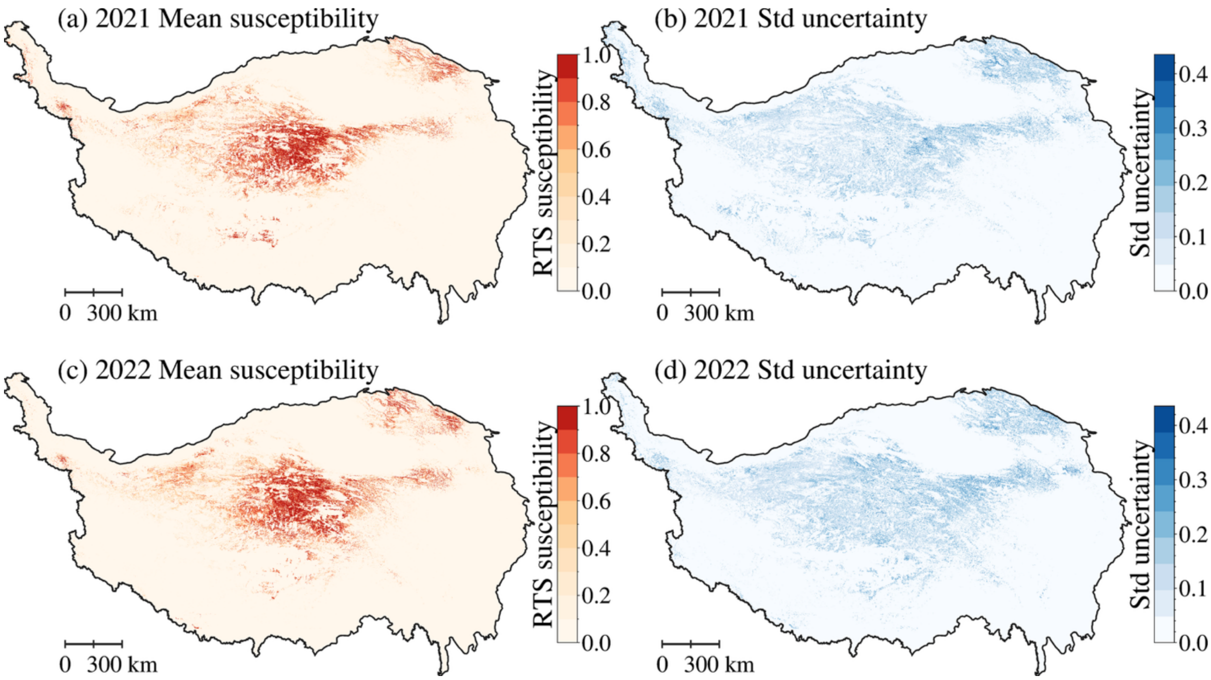

Fig. 7 Spatial distribution of predicted RTS susceptibility (a, c) and prediction standard deviation (b, d) for 2021 (top row) and 2022 (bottom row), based on the five-fold ensemble of Model 3.

https://doi.org/10.5194/egusphere-2026-5035
Preprint. Discussion started: 18 September 2026

4.4 Model Interpretation via SHAP Analysis

SHAP analysis was conducted on Model 3 to quantify the contribution of each environmental predictor and interpret their associations with predicted RTS susceptibility. As shown in Fig. 8, NDVI was the most influential predictor, followed by slope, ground ice content (GIC), and vegetation type. These four variables represent the primary set of predisposing factors within the model. Secondary contributors included dynamic hydroclimatic variables such as thawing degree days (TDD), warm-season relative humidity (WSRH), and summer soil moisture, reflecting their contribution to interannual variability in susceptibility.

The beeswarm plot in Fig. 8 reveals both the magnitude and direction of each predictor's influence. Higher NDVI values were strongly associated with lower susceptibility, consistent with general stabilizing influence of vegetation cover. Slope showed a positive contribution within a moderate range, while GIC exhibited a pronounced positive association above approximately 21%. Vegetation type displayed strong categorical effects, with alpine steppe and meadow associated with higher susceptibility and dense shrubland or forest associated with lower susceptibility.

Detailed SHAP dependence plots (Supplementary Fig. S11) further revealed nonlinear and threshold-like responses for most predictors. Notable patterns include a transition in NDVI near 0.16–0.23, a unimodal response for slope with peak susceptibility between approximately 4.6° and 25°, and an increased response of GIC above approximately 21% before reaching a plateau. These threshold-like patterns describe nonlinear associations between the predictors and modelled RTS susceptibility across the QTP.

Overall, the SHAP results indicate that RTS susceptibility is primarily associated with a relatively stable combination of predisposing factors consisting of vegetation cover, terrain steepness, and ground ice content, with annual hydroclimatic conditions serving as important secondary contributors.

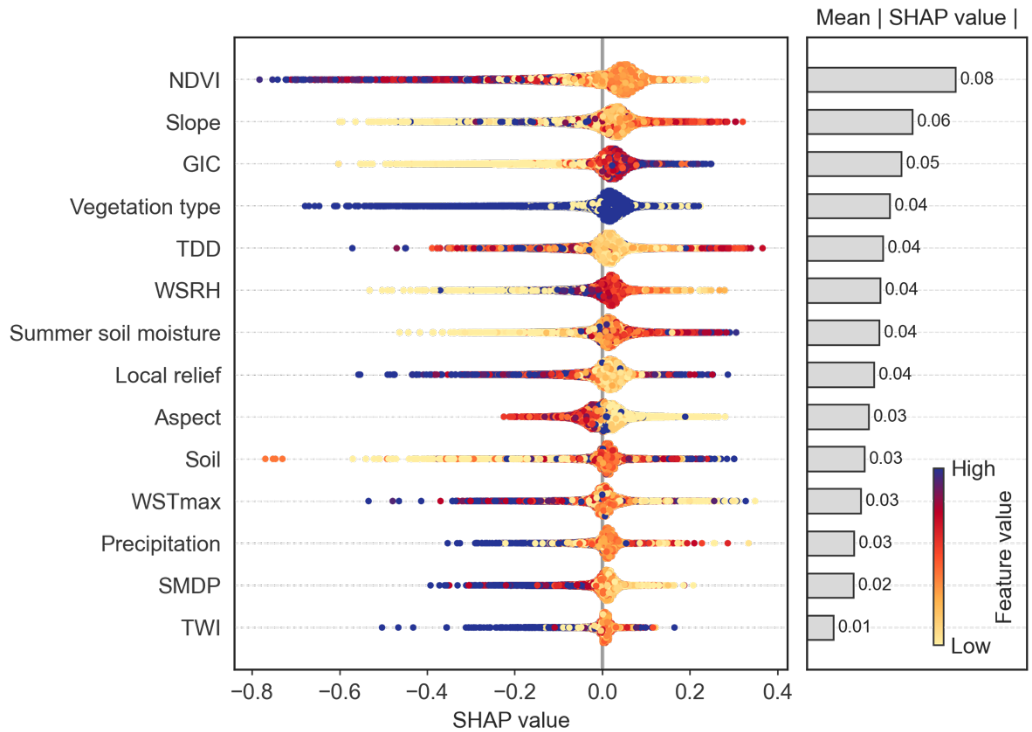

Fig. 8 Global SHAP feature importance for Model 3. The left panel shows the beeswarm plot of SHAP values for all 14 predictors, with points colored by feature value. The right panel displays the mean absolute SHAP values, indicating the overall contribution of each predictor to the model output. NDVI, slope, ground ice content (GIC), and vegetation type are identified as the four most influential predictors in the model.

5 Discussion

5.1 Initiation Timing as Weak Supervision for Forward-Looking Susceptibility

The most consequential difference among the three models emerged not in cross-validation, where their performance was nearly identical, but in the temporally held-out evaluation. The substantially stronger concentration of subsequent RTS initiations in the upper susceptibility tail of the Annual-YBI model indicates that temporal-order supervision adds information that conventional binary discrimination does not fully reveal. This distinction matters for susceptibility mapping because a model can reproduce historical occurrence patterns well without necessarily ranking locations prone to future initiation equally well.

The temporal-validation result supports, but does not prove, the premise underlying YBI: within locally comparable settings, initiation order contains useful information about relative pre-initiation susceptibility. YBI should not be interpreted as a direct measurement of physical instability or as an estimate of time to failure. RTS initiation also depends on short-lived

https://doi.org/10.5194/egusphere-2026-5035
Preprint. Discussion started: 18 September 2026

triggers and local conditions that are not resolved by annual predictors, so the ordering represents a probabilistic source of weak supervision rather than a deterministic sequence toward failure.

The controlled comparison between the Annual Binary and Annual-YBI models helps isolate this contribution. Because both use the same year-specific environmental predictors, their difference in forward performance indicates that temporal information can improve susceptibility modeling not only through dynamic predictors but also through the supervision structure itself. This finding directly addresses the limitation of binary classification identified in previous susceptibility studies, in which pre-initiation observations are either unused or treated simply as non-event background (Huang et al., 2024).

The advantage of DBSCAN-based local comparability domains further suggests that initiation order is not universally comparable across the QTP. Its information content appears conditional on environmental context: ordering locations within broadly similar settings is more defensible than imposing a plateau-wide sequence across contrasting climatic, topographic, vegetation, and permafrost regimes. Local ranking cannot eliminate all such heterogeneity, but it reduces the risk that geographic contrasts are mistaken for temporal differences in susceptibility. This conditional interpretation is also important when considering transfer of the framework to other regions.

The improvement in forward ranking was achieved with only modest changes in the spatial extent of high-susceptibility zones. Thus, the Annual-YBI model did not improve event capture simply by assigning high susceptibility to a larger fraction of the landscape; instead, it concentrated higher susceptibility more effectively around locations that subsequently initiated. For regional screening, this ability to improve prioritization within the upper tail of the susceptibility distribution may be more useful than a general upward shift in predicted susceptibility.

5.2 Environmental Controls and Spatial Expression of RTS Susceptibility

The susceptibility patterns generated in this study show broad spatial consistency with previous QTP-wide assessments. Very high susceptibility zones are concentrated in the central permafrost region and broadly correspond to the active RTS clusters documented by Xia et al. (2024b) and previous QTP-wide mapping studies (Yin et al., 2021; Zhu et al., 2026b). This convergence is consistent with the importance of terrain steepness, ground ice content, and vegetation cover as key predisposing factors.

Previous work has highlighted the importance of slope and meteorological conditions (He et al., 2024; Wang et al., 2024). Our SHAP results point to a distinction between relatively persistent spatial predisposition and interannual environmental modulation. Vegetation cover, terrain steepness, and ground ice content largely define where susceptible settings occur, whereas year-specific hydroclimatic conditions modify susceptibility within this broader environmental template. These patterns are broadly consistent with established physical controls on RTS development in ice-rich permafrost (Li et al., 2024) and with nonlinear water–heat–vegetation interactions on the QTP (Ji et al., 2025; Lin et al., 2025).

The lower global SHAP importance of annual hydroclimatic variables therefore should not be interpreted as evidence that climate forcing is unimportant for RTS initiation. Their influence may be expressed more strongly through the timing of failure on already predisposed terrain than through the broad spatial pattern of susceptibility, while their relatively coarse

https://doi.org/10.5194/egusphere-2026-5035
Preprint. Discussion started: 18 September 2026

spatial resolution may further reduce their apparent contribution at local scales. SHAP values also describe associations within the fitted model and should not be interpreted as direct causal effects of individual environmental variables.

For comparison with previous mapping studies, we aggregated the 2021 and 2022 Annual-YBI predictions into a 2021–2022 maximum susceptibility composite (Fig. 9) Using the standardized permafrost extent of Cao et al. (2023) (1.086×10^6 km^2), the composite classified approximately 1.70×10^5 km^2 (15.6%) as high or very high susceptibility. This extent is larger than that mapped by Yin et al. (2021) (1.60×10^4 km^2, 1.5%) and lies above the range reported by several current-climate models of Zhu et al. (2026b) (5.97×10^4–1.12×10^5 km^2, 5.5%–10.3%), but these differences should not be interpreted as direct temporal changes in susceptibility. They reflect differences in inventory coverage and timing, mapped process, susceptibility definition, model formulation, and in our case, the use of the pixel-wise maximum of two annual predictions. The broader and more recent annual inventory of Xia et al. (2024a) also documents substantial growth in RTS number (1.4-fold) and affected area (2.8-fold) between 2016 and 2022.

At basin scale, the Inner Plateau and Yangtze basins together accounted for 78.5% of the areas classified as high or very high susceptibility across the 12 basin summaries (Fig. 9a). This concentration indicates that high RTS susceptibility is spatially clustered rather than uniformly distributed across QTP permafrost. Independent geodetic observations provide additional spatial corroboration: the subsidence hotspots reported by Guo et al. (2026) show substantial spatial correspondence with areas mapped here as having very highly susceptible. This correspondence is encouraging, but subsidence represents complementary evidence of ground instability rather than an independent validation of RTS initiation susceptibility itself.

https://doi.org/10.5194/egusphere-2026-5035
Preprint. Discussion started: 18 September 2026

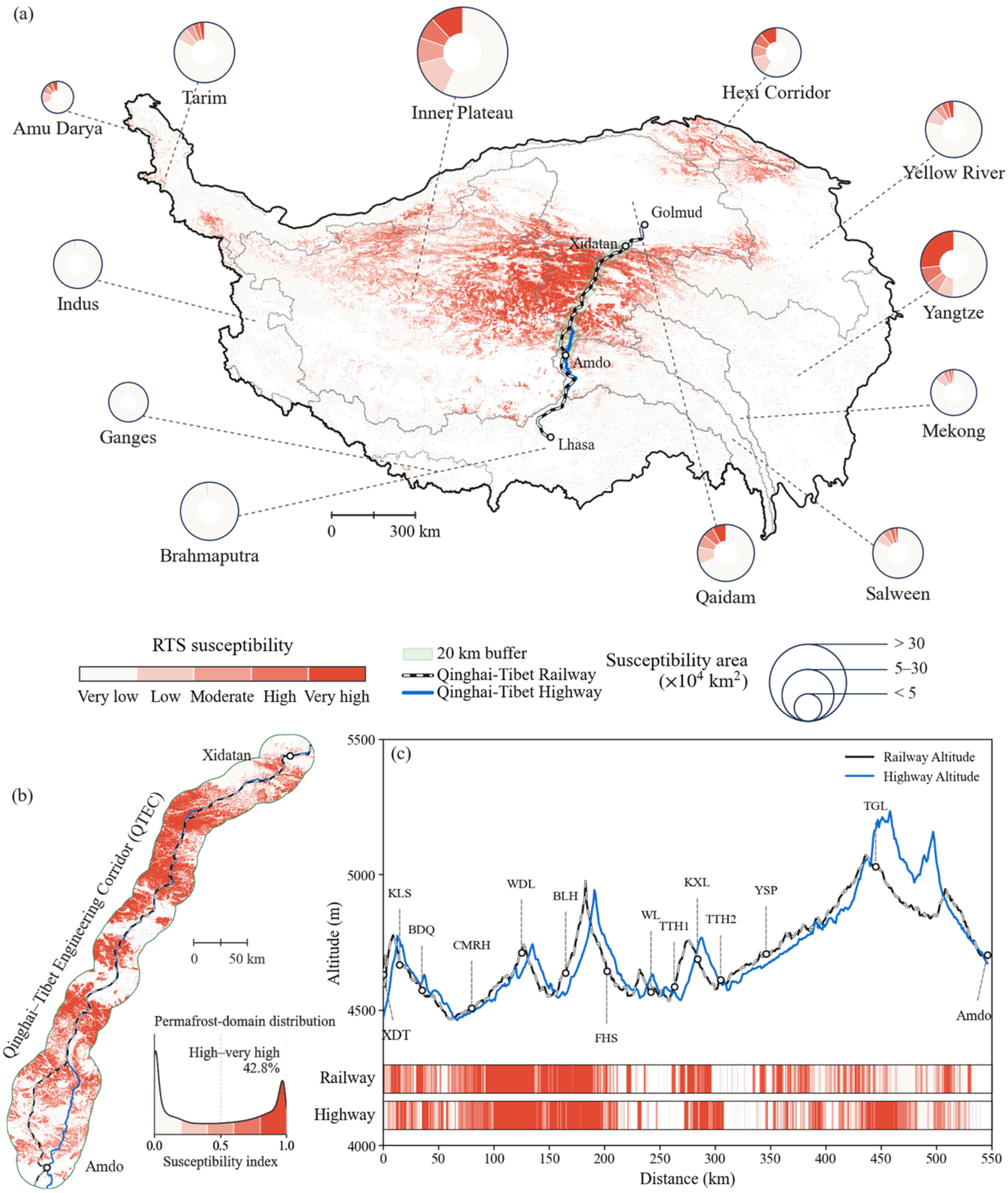

485

Fig. 9 Plateau- and corridor-scale distribution of the 2021–2022 maximum RTS susceptibility composite, with local susceptibility along the railway and highway. The composite was generated by taking the pixel-wise maximum of the independently predicted annual susceptibility maps for 2021 and 2022, both derived from the five-fold ensemble of Model 3. (a) Spatial distribution and class composition of susceptibility across 12 major Qinghai–Tibet Plateau basins. Donut sectors show the proportions of the five susceptibility classes, and symbol size represents the mapped area included in each basin summary. (b) Susceptibility distribution within the 20-km Qinghai–Tibet Engineering Corridor buffer and the kernel-density curve of susceptibility values. The annotated 42.8% denotes the proportion of mapped permafrost area within the buffer classified as high or very high susceptibility (≥ 0.6). (c)

https://doi.org/10.5194/egusphere-2026-5035
Preprint. Discussion started: 18 September 2026

SRTM elevation profiles and local susceptibility along the Xidatan–Amdo railway and highway sectors. Susceptibility ribbons show the P90 value within a 500-m-radius circular buffer evaluated at 100-m intervals.

5.3 Implications for Susceptibility Screening and Monitoring

The spatial concentration of predicted susceptibility has direct implications for regional screening and monitoring along the QTEC. Within the 20-km QTEC buffer, zones of high or very high susceptibility covered approximately 8.6 × 10^3 km^2, equivalent to 42.8% of the mapped permafrost (Fig. 9b). At the route scale, 52.56% of sampled railway positions and 58.08% of sampled highway positions met the high-susceptibility threshold (≥ 0.6; Fig. 9c) based on the 90th percentile of susceptibility within 500-m local buffers. These percentages should be interpreted as indicators of where more detailed investigation may be warranted, rather than as estimates of infrastructure risk. Susceptibility describes the relative spatial propensity for RTS initiation, whereas risk additionally depends on event probability, magnitude, exposure, vulnerability, and consequences, none of which are explicitly modeled here. The corridor analysis is therefore most appropriately used to prioritize field inspection, geotechnical investigation, remote-sensing surveillance, and other monitoring efforts rather than to infer site-specific engineering safety.

Prediction uncertainty provides an additional basis for such prioritization. Ensemble variability was generally low across the QTP, but uncertainty increased toward the most susceptible terrain and in environmentally heterogeneous transition zones. Areas combining high susceptibility with low ensemble variability represent relatively robust screening targets, whereas high-susceptibility areas with greater model disagreement warrant additional observations before management decisions are made. At the same time, the five-fold ensemble standard deviation used here measures sensitivity to training-data partitioning rather than the full uncertainty associated with inventories, environmental predictors, model structure, and future forcing. The uncertainty maps should therefore be interpreted as model-consistency diagnostics rather than complete probabilistic uncertainty estimates.

More broadly, the results demonstrate the added value of preserving temporal structure when increasingly detailed annual permafrost inventories are converted into susceptibility information. The benefit is not simply that more samples become available; rather, known initiation times provide an additional relationship among samples that conventional binary labels discard. This distinction makes temporal-order supervision potentially useful for other progressively developing mass-movement processes where multi-year initiation inventories are available, while avoiding the stronger data requirements of fully process-based forecasting.

5.4 Limitations and Future Directions

Several limitations and sources of uncertainty should be considered when interpreting these results. First, the annual inventory records the year of first detection, which is used as a proxy for initiation year; actual initiation may precede detection because of image availability, seasonal observation windows, mapping uncertainty, or delayed surface expression (Ozturk et

https://doi.org/10.5194/egusphere-2026-5035
Preprint. Discussion started: 18 September 2026

al., 2021). Such timing errors directly affect YBI and therefore the ordering constraints. Denser image time series or probabilistic representations of initiation timing could reduce the need to treat annual detection year as exact.

Second, the assumption that earlier initiation implies greater relative susceptibility is intentionally weak rather than deterministic. Extreme precipitation, anomalous warmth, local hydrological change, or unrepresented disturbances may cause a less predisposed slope to fail earlier than another slope. Restricting ranking pairs to local DBSCAN domains reduces inappropriate comparisons, but cannot remove all heterogeneity in triggering conditions or geological context. Future work could therefore examine probabilistic ranking formulations and quantify how uncertainty in initiation order propagates into susceptibility predictions.

Pseudo-absence sampling, even with a 1,000-m exclusion buffer, may still involve label contamination, and the lack of true negative samples remains a well-known challenge in susceptibility modeling (Chang et al., 2023; Huang et al., 2024). Moreover, sites that have not initiated during the inventory period are not necessarily stable negatives; some may simply be right-censored locations that could fail later. Time-to-event or discrete-time survival formulations would provide a useful future benchmark because they can treat such censoring explicitly and could be compared directly with the simpler weak-ranking strategy developed here. The present pseudo-absence pool was also screened against the complete 2016–2022 inventory so that known 2021–2022 RTS sites were not inadvertently used as training negatives. Although this provides a clean temporally held-out evaluation, it is more informed than a strictly prospective setting in which future initiation sites are unknown. Future tests should therefore evaluate alternative background-sampling strategies under prospective conditions.

Third, the relatively coarse resolution of hydroclimatic forcings (ERA5-Land at 11.1 km and SMAP at 9 km) compared with the 100-m analysis grid limits the representation of fine-scale hydrological heterogeneity relevant for slope stability (Fu et al., 2025). In addition, annual aggregates cannot fully resolve short-lived triggers such as intense rainfall, heat waves, rapid snowmelt, or episodic changes in soil moisture. Incorporating daily or event-scale forcing could help separate persistent predisposition from triggering conditions. High-resolution interferometric synthetic aperture radar (InSAR) coherence and deformation time series could further provide direct evidence of pre-initiation surface change while reducing the scale mismatch between dynamic predictors and mapped slopes (Song et al., 2025).

Another priority is to move beyond independent grid-cell prediction. RTS initiation and subsequent sediment and water redistribution occur within connected hillslope and drainage systems, whereas the present framework treats pixels independently. Coupling temporal-order supervision with lateral-connectivity approaches such as COHESION (Schmitt et al., 2025) could extend the present pixel-based framework toward hillslope- or watershed-scale representations and provide a basis for examining feedbacks between RTS development and hydrological connectivity(Yang et al., 2019).

Transfer to other permafrost regions is promising but should not be assumed to be straightforward. The QTP differs from high-latitude Arctic environments in ground temperature, permafrost thickness, topography, vegetation, and climatic forcing (Lewkowicz and Way, 2019; Segal et al., 2016; Strauss et al., 2017; Yang et al., 2010; You et al., 2022; Zhao et al., 2024). Spatial comparability scales, environmental predictors, and temporal forcing variables should therefore be recalibrated locally. Testing the framework against independent annual inventories outside the QTP would be particularly valuable for establishing

https://doi.org/10.5194/egusphere-2026-5035
Preprint. Discussion started: 18 September 2026

whether the benefit of temporal-order supervision is region-specific or generalizable.Finally, linking this susceptibility framework with process-based evolution models such as RTSEvo (Xu et al., 2026) could enable an integrated modeling chain from identifying initiation-prone locations to simulating post-failure growth and hazard evolution.

6 Conclusions

This study demonstrates that the timing of RTS initiation contains useful susceptibility information that is lost when multi-year inventories are reduced to binary occurrence labels. To exploit this information, we developed the Annual-YBI model, a weakly supervised framework that represents initiation timing as Years Before Initiation (YBI) and uses the resulting temporal order to distinguish relative pre-initiation susceptibility.

Although all three models performed almost identically in five-fold cross-validation (ROC-AUC ≈ 0.988), their forward-looking performance differed substantially. The proposed Annual-YBI model captured 89.45% of 199 temporally held-out 2021–2022 RTS initiations within the top 10% susceptibility area. In comparison, the two conventional binary baselines, one using temporally aggregated predictors (Static Binary) and the other using year-specific predictors but binary supervision only (Annual Binary), captured 63.82% and 79.90%, respectively. This contrast indicates that initiation-time ordering contributes primarily to ranking locations prone to subsequent initiation rather than to improving discrimination of historical binary classes.

Across the QTP, vegetation cover, slope, and ground ice content emerged as the principal spatial predisposing factors, while annual hydroclimatic conditions provided additional interannual modulation. The 2021–2022 maximum susceptibility composite classified approximately 1.70×10^5 km² (15.6% of QTP permafrost) as high or very high susceptibility, with the Inner Plateau and Yangtze basins accounting for 78.5% of this area. Within the 20-km Qinghai–Tibet Engineering Corridor buffer, 42.8% of mapped permafrost was classified as high or very high susceptibility, highlighting priority areas for further investigation and monitoring rather than constituting a direct estimate of infrastructure risk.

The results show that time-stamped inventories provide more than repeated binary observations: their initiation sequence can serve as an ordinal supervision signal for resolving susceptibility gradients before visible failure. With improved constraints on initiation timing, triggering conditions, and local spatial comparability, the approach could be extended to other permafrost regions and to other progressively developing mass-movement processes for which multi-year initiation records are available.

Code and data availability

The code used in this study is archived on Zenodo (Li and Nan, 2026; https://doi.org/10.5281/zenodo.20603769). The predicted 2021 and 2022 RTS susceptibility maps (100 m) can be interactively viewed via Google Earth Engine at https://summer-presence-475413-i4.projects.earthengine.app/view/qtprtssusceptibilitymapping (accessed 12 August 2026). The annual RTS inventories are archived on Zenodo (Xia et al., 2024a; https://doi.org/10.5281/zenodo.10928346). The 2010 permafrost distribution map over the QTP is available through Figshare (Cao, 2023; https://doi.org/10.6084/m9.figshare.19642362.v5), and the ground-ice content dataset is available through the National Tibetan Plateau Data Center (Zou et al., 2024b; https://doi.org/10.11888/Cryos.tpdc.300748). The TP_LC10 land-cover dataset is archived on Zenodo (Huang et al., 2023; https://doi.org/10.5281/zenodo.10875021). Topographic variables were derived from the CGIAR-CSI SRTM Version 4 dataset (Jarvis et al., 2008; https://bigdata.cgiar.org/srtm-90m-digital-elevation-database/) and HydroSHEDS (Lehner et al., 2008; https://www.hydrosheds.org/products/hydrosheds). Soil fine-fraction data were obtained from SoilGrids 2.0 (Poggio et al., 2021; https://soilgrids.org/), and NDVI data were obtained from the MODIS/Terra Vegetation Indices 16-Day L3 Global 250 m SIN Grid V061 product (Didan, 2021; https://doi.org/10.5067/MODIS/MOD13Q1.061). Hydroclimatic variables were derived from ERA5-Land hourly data (Muñoz Sabater, 2019; https://doi.org/10.24381/cds.e2161bac), and soil-moisture data were obtained from the SMAP Enhanced L3 Radiometer Global and Polar Grid Daily 9 km EASE-Grid Soil Moisture, Version 6 product (O'Neill et al., 2023; https://doi.org/10.5067/M20OXIZHY3RJ).

Author contributions

PL: Data curation; Formal analysis; Methodology; Software; Validation; Visualization; Writing – original draft; Writing – review & editing. ZN: Conceptualization; Funding acquisition; Methodology; Resources; Supervision; Writing – original draft; Writing – review & editing. JX: Data curation; Software; Validation. FN: Funding acquisition; Writing – review & editing

Competing interests

The authors declare that they have no conflicts of interest.

Acknowledgements

This study was supported by the Science and Technology Project of Qinghai Provincial Department of Transportation (JG2024-83) and the National Natural Science Foundation of China (No. 42571149).

References

Barth, S., Nitze, I., Juhls, B., Runge, A., and Grosse, G.: Rapid changes in retrogressive thaw slump dynamics in the Russian High Arctic based on very high-resolution remote sensing, Geophys. Res. Lett., 52, e2024GL113022, https://doi.org/10.1029/2024GL113022, 2025.

Burges, C. J. C., Ragno, R., and Le, Q. V.: Learning to rank with nonsmooth cost functions, in: Advances in Neural

Information Processing Systems 19, edited by: Schölkopf, B., Platt, J., and Hofmann, T., The MIT Press, Cambridge, MA, 193–200, https://doi.org/10.7551/mitpress/7503.003.0029, 2007.

Cao, Z.: Dataset associated with the article "A new 2010 permafrost distribution map over the Qinghai–Tibet Plateau based on subregion survey maps: A benchmark for regional permafrost modelling" published on Earth System Science Data (5), Figshare [data set], https://doi.org/10.6084/m9.figshare.19642362.v5, 2023.

Cao, Z., Nan, Z., Hu, J., Chen, Y., and Zhang, Y.: A new 2010 permafrost distribution map over the Qinghai–Tibet Plateau based on subregion survey maps: A benchmark for regional permafrost modeling, Earth Syst. Sci. Data, 15, 3905–3930, https://doi.org/10.5194/essd-15-3905-2023, 2023.

Chang, Z., Huang, J., Huang, F., Bhuyan, K., Meena, S. R., and Catani, F.: Uncertainty analysis of non-landslide sample selection in landslide susceptibility prediction using slope unit-based machine learning models, Gondwana Res., 117, 307–320, https://doi.org/10.1016/j.gr.2023.02.007, 2023.

Chaudhary, P., D'Aronco, S., Leitão, J. P., Schindler, K., and Wegner, J. D.: Water level prediction from social media images with a multi-task ranking approach, ISPRS J. Photogramm. Remote Sens., 167, 252–262, https://doi.org/10.1016/j.isprsjprs.2020.07.003, 2020.

Chen, D., Xu, B., Yao, T., Guo, Z., Cui, P., Chen, F., Zhang, R., Zhang, X., Zhang, Y., Fan, J., Hou, Z., and Zhang, T.: Assessment of past, present and future environmental changes on the Tibetan Plateau (in Chinese), Chin. Sci. Bull., 60, 3025–3035, https://doi.org/10.1360/N972014-01370, 2015.

Cheng, G. and Wu, T.: Responses of permafrost to climate change and their environmental significance, Qinghai-Tibet Plateau, J. Geophys. Res. Earth Surf., 112, F02S03, https://doi.org/10.1029/2006JF000631, 2007.

Didan, K.: MODIS/Terra vegetation indices 16-day L3 global 250m SIN grid V061, NASA Land Processes Distributed Active Archive Center [data set], https://doi.org/10.5067/MODIS/MOD13Q1.061, 2021.

Entekhabi, D., Njoku, E. G., O'Neill, P. E., Kellogg, K. H., Crow, W. T., Edelstein, W. N., Entin, J. K., Goodman, S. D., Jackson, T. J., Johnson, J., Kimball, J., Piepmeier, J. R., Koster, R. D., Martin, N., McDonald, K. C., Moghaddam, M., Moran, S., Reichle, R., Shi, J. C., Spencer, M. W., Thurman, S. W., Tsang, L., and Van Zyl, J.: The soil moisture active passive (SMAP) mission, Proc. IEEE, 98, 704–716, https://doi.org/10.1109/JPROC.2010.2043918, 2010.

Fan, X., Lin, Z., Yao, M., Wang, Y., Gu, Q., Luo, J., Wu, X., and Gao, Z.: Spatio-temporal evolution and susceptibility assessment of thaw slumps associated with climate change in the Hoh Xil region, in the hinterland of the Qinghai–Tibet Plateau, Remote Sens., 17, 1614, https://doi.org/10.3390/rs17091614, 2025.

French, H. M.: The periglacial environment, 4th ed., John Wiley & Sons, Hoboken, NJ, https://doi.org/10.1002/9781119132820, 2017.

Fu, Z., Wu, Q., Chen, A., Wang, L., Jiang, G., Gao, S., Yun, H., and Chen, J.: Non-temperature environmental drivers modulate warming-induced 21st-century permafrost degradation on the Tibetan Plateau, Nat. Commun., 16, 7556, https://doi.org/10.1038/s41467-025-63032-x, 2025.

Guo, H., Zou, L., Wang, C., Li, X., Tang, Y., Zhang, Z., Ma, P., Wu, F., and Zhang, H.: Satellite radar reveals nearly 20%

https://doi.org/10.5194/egusphere-2026-5035
Preprint. Discussion started: 18 September 2026

permafrost undergoing interannual subsidence in the Tibetan Plateau, Sci. Bull., 71, 3597–3599, https://doi.org/10.1016/j.scib.2026.02.051, 2026.

Guzzetti, F., Reichenbach, P., Cardinali, M., Galli, M., and Ardizzone, F.: Probabilistic landslide hazard assessment at the basin scale, Geomorphology, 72, 272–299, https://doi.org/10.1016/j.geomorph.2005.06.002, 2005.

Guzzetti, F., Mondini, A. C., Cardinali, M., Fiorucci, F., Santangelo, M., and Chang, K.-T.: Landslide inventory maps: New tools for an old problem, Earth-Sci. Rev., 112, 42–66, https://doi.org/10.1016/j.earscirev.2012.02.001, 2012.

He, Y., Huo, T., Gao, B., Zhu, Q., Jin, L., Chen, J., Zhang, Q., and Tang, J.: Thaw slump susceptibility mapping based on sample optimization and ensemble learning techniques in Qinghai-Tibet Railway corridor, IEEE J. Sel. Top. Appl. Earth Obs. Remote Sens., 17, 5443–5459, https://doi.org/10.1109/JSTARS.2024.3368039, 2024.

Huang, F., Mao, D., Jiang, S.-H., Zhou, C., Fan, X., Zeng, Z., Catani, F., Yu, C., Chang, Z., Huang, J., Jiang, B., and Li, Y.: Uncertainties in landslide susceptibility prediction modeling: A review on the incompleteness of landslide inventory and its influence rules, Geosci. Front., 15, 101886, https://doi.org/10.1016/j.gsf.2024.101886, 2024.

Huang, X., Yin, Y., Feng, L., Tong, X., Zhang, X., Li, J., and Tian, F.: A 10 m resolution land cover map of the Tibetan Plateau with detailed vegetation types, Zenodo [data set], https://doi.org/10.5281/zenodo.10875021, 2023.

Jarvis, A., Reuter, H. I., Nelson, A., and Guevara, E.: Hole-filled SRTM for the globe version 4, CGIAR-CSI SRTM 90m Database [data set], https://srtm.csi.cgiar.org/, 2008.

Jenks, G. F.: The data model concept in statistical mapping, Int. Yearb. Cartogr., 7, 186–190, 1967.

Ji, F., Yuan, S., Fan, L., Zhu, L., Jin, J., Yao, Y., Liu, Y., Guan, T., Zheng, C., and Zhang, J.: Thresholds in land-atmosphere interactions on the Qinghai-Tibet Plateau: impacts of permafrost degradation via vegetation changes, J. Hydrol., 662, 133912, https://doi.org/10.1016/j.jhydrol.2025.133912, 2025.

Ji, H., Wu, X., Zhao, S., and Nan, Z.: Constrained simulation of permafrost thermal changes from 1980 to 2018 on the Qinghai-Tibet Plateau, Glob. Planet. Change, 263, 105542, https://doi.org/10.1016/j.gloplacha.2026.105542, 2026.

Kokelj, S. V. and Jorgenson, M. T.: Advances in thermokarst research, Permafr. Periglac. Process., 24, 108–119, https://doi.org/10.1002/ppp.1779, 2013.

Lehner, B., Verdin, K., and Jarvis, A.: New global hydrography derived from spaceborne elevation data, Eos Trans. Am. Geophys. Union, 89, 93–94, https://doi.org/10.1029/2008EO100001, 2008.

Lewkowicz, A. G. and Way, R. G.: Extremes of summer climate trigger thousands of thermokarst landslides in a High Arctic environment, Nat. Commun., 10, 1329, https://doi.org/10.1038/s41467-019-09314-7, 2019.

Li, P. and Nan, Z.: nanzt/YBIRTS-Susceptibility: v1.0.0, Zenodo [code], https://doi.org/10.5281/zenodo.20603769, 2026.

Li, Y., Liu, Y., Chen, J., Dang, H., Zhang, S., Mei, Q., Zhao, J., Wang, J., Dong, T., and Zhao, Y.: Advances in retrogressive thaw slump research in permafrost regions, Permafr. Periglac. Process., 35, 125–142, https://doi.org/10.1002/ppp.2218, 2024.

Lin, X., Wu, T., Chen, J., Chen, J., Li, R., Zhu, X., and Lou, P.: Revealing the impacts of environmental and anthropogenic factors on permafrost deformation in the central Qinghai-Tibet Plateau using InSAR and interpretable machine learning, Ecol. Indic., 178, 113977, https://doi.org/10.1016/j.ecolind.2025.113977, 2025.

Lundberg, S. M. and Lee, S.-I.: A unified approach to interpreting model predictions, in: Advances in Neural Information Processing Systems, 31st Conference on Neural Information Processing Systems (NIPS 2017), Long Beach, CA, USA, 4-9 December 2017, 4765–4774, 2017.

Luo, J., Yin, G.-A., Niu, F.-J., Dong, T.-C., Gao, Z.-Y., Liu, M.-H., and Yu, F.: Machine learning-based predictions of current and future susceptibility to retrogressive thaw slumps across the Northern Hemisphere, Adv. Clim. Change Res., 15, 253–264, https://doi.org/10.1016/j.accre.2024.03.001, 2024.

Ma, P., Chen, L., Yu, C., Zhu, Q., Ding, Y., Wu, Z., Li, H., Tian, C., and Fan, X.: Dynamic landslide susceptibility mapping over last three decades to uncover variations in landslide causation in subtropical urban mountainous areas, Remote Sens. Environ., 326, 114800, https://doi.org/10.1016/j.rse.2025.114800, 2025.

Makopoulou, E., Karjalainen, O., Elia, L., Blais-Stevens, A., Lantz, T., Lipovsky, P., Lombardo, L., Nicu, I. C., Rubensdotter, L., Rudy, A. C. A., and Hjort, J.: Retrogressive thaw slump susceptibility in the northern hemisphere permafrost region, Earth Surf. Process. Landf., 49, 3319–3331, https://doi.org/10.1002/esp.5890, 2024.

Muñoz Sabater, J.: ERA5-Land hourly data from 1950 to present, Copernicus Climate Change Service (C3S) Climate Data Store (CDS) [data set], https://doi.org/10.24381/CDS.E2161BAC, 2019.

Muñoz-Sabater, J., Dutra, E., Agustí-Panareda, A., Albergel, C., Arduini, G., Balsamo, G., Boussetta, S., Choulga, M., Harrigan, S., and Hersbach, H.: ERA5-Land: A state-of-the-art global reanalysis dataset for land applications, Earth Syst. Sci. Data, 13, 4349–4383, https://doi.org/10.5194/essd-13-4349-2021, 2021.

Nesterova, N., Leibman, M., Kizyakov, A., Lantuit, H., Tarasevich, I., Nitze, I., Veremeeva, A., and Grosse, G.: Review article: Retrogressive thaw slump characteristics and terminology, The Cryosphere, 18, 4787–4810, https://doi.org/10.5194/tc-18-4787-2024, 2024.

O'Neill, P., Chan, S., Njoku, E., Jackson, T., Bindlish, R., Chaubell, J., and Colliander, A.: SMAP enhanced L3 radiometer global and polar grid daily 9 km EASE-grid soil moisture, version 6, NASA National Snow and Ice Data Center Distributed Active Archive Center [data set], https://doi.org/10.5067/M20OXIZHY3RJ, 2023.

Ozturk, U., Pittore, M., Behling, R., Roessner, S., Andreani, L., and Korup, O.: How robust are landslide susceptibility estimates?, Landslides, 18, 681–695, https://doi.org/10.1007/s10346-020-01485-5, 2021.

Poggio, L., De Sousa, L. M., Batjes, N. H., Heuvelink, G. B. M., Kempen, B., Ribeiro, E., and Rossiter, D.: SoilGrids 2.0: Producing soil information for the globe with quantified spatial uncertainty, SOIL, 7, 217–240, https://doi.org/10.5194/soil-7-217-2021, 2021.

Reichenbach, P., Rossi, M., Malamud, B. D., Mihir, M., and Guzzetti, F.: A review of statistically-based landslide susceptibility models, Earth-Sci. Rev., 180, 60–91, https://doi.org/10.1016/j.earscirev.2018.03.001, 2018.

Schmitt, R. J. P., Bhandari, S., Vogl, A., and Marc, O.: Leveraging hillslope connectivity for improved large-scale assessments of landslide risk, EGUsphere [preprint], https://doi.org/10.5194/egusphere-2025-3733, 15 October 2025.

Segal, R. A., Lantz, T. C., and Kokelj, S. V.: Acceleration of thaw slump activity in glaciated landscapes of the Western

https://doi.org/10.5194/egusphere-2026-5035
Preprint. Discussion started: 18 September 2026

Canadian Arctic, Environ. Res. Lett., 11, 034025, https://doi.org/10.1088/1748-9326/11/3/034025, 2016.

Song, Y., Hu, X., Shi, X., Cui, Y., Zhou, C., and Xu, Y.: Hydrological proxy derived from InSAR coherence in landslide characterization, Remote Sens. Environ., 322, 114712, https://doi.org/10.1016/j.rse.2025.114712, 2025.

Strauss, J., Schirrmeister, L., Grosse, G., Fortier, D., Hugelius, G., Knoblauch, C., Romanovsky, V., Schädel, C., Schneider von Deimling, T., Schuur, E. A. G., Shmelev, D., Ulrich, M., and Veremeeva, A.: Deep Yedoma permafrost: A synthesis of depositional characteristics and carbon vulnerability, Earth-Sci. Rev., 172, 75–86, https://doi.org/10.1016/j.earscirev.2017.07.007, 2017.

Wang, F., Wen, Z., Gao, Q., Yu, Q., Li, D., and Chen, L.: Thermokarst landslides susceptibility evaluation across the permafrost region of the central Qinghai-Tibet Plateau: Integrating a machine learning model with InSAR technology, J. Hydrol., 642, 131800, https://doi.org/10.1016/j.jhydrol.2024.131800, 2024.

Xia, Z., Liu, L., Mu, C., Peng, X., Zhao, Z., Huang, L., Luo, J., and Fan, C.: Annual inventories of retrogressive thaw slumps across the Qinghai-Tibet Plateau from 2016 to 2022, Zenodo [data set], https://doi.org/10.5281/zenodo.10928346, 2024a.

Xia, Z., Liu, L., Mu, C., Peng, X., Zhao, Z., Huang, L., Luo, J., and Fan, C.: Widespread and rapid activities of retrogressive thaw slumps on the Qinghai-Tibet Plateau from 2016 to 2022, Geophys. Res. Lett., 51, e2024GL109616, https://doi.org/10.1029/2024GL109616, 2024b.

Xu, J., Zhao, S., Nan, Z., Niu, F., and Zhang, Y.: RTSEvo v1.0: A retrogressive thaw slump evolution model, Geosci. Model Dev., 19, 2919–2943, https://doi.org/10.5194/gmd-19-2919-2026, 2026.

Yang, M., Nelson, F. E., Shiklomanov, N. I., Guo, D., and Wan, G.: Permafrost degradation and its environmental effects on the Tibetan Plateau: A review of recent research, Earth-Sci. Rev., 103, 31–44, https://doi.org/10.1016/j.earscirev.2010.07.002, 2010.

Yang, Y., Wu, Q., Jin, H., Wang, Q., Huang, Y., Luo, D., Gao, S., and Jin, X.: Delineating the hydrological processes and hydraulic connectivities under permafrost degradation on Northeastern Qinghai-Tibet Plateau, China, J. Hydrol., 569, 359–372, https://doi.org/10.1016/j.jhydrol.2018.11.068, 2019.

Yin, G., Luo, J., Niu, F., Lin, Z., and Liu, M.: Machine learning-based thermokarst landslide susceptibility modeling across the permafrost region on the Qinghai-Tibet Plateau, Landslides, 18, 2639–2649, https://doi.org/10.1007/s10346-021-01669-7, 2021.

You, Y., Guo, L., Yu, Q., Wang, X., Pan, X., Wu, Q., Wang, D., and Wang, G.: Spatial variability and influential factors of active layer thickness and permafrost temperature change on the Qinghai-Tibet Plateau from 2012 to 2018, Agric. For. Meteorol., 318, 108913, https://doi.org/10.1016/j.agrformet.2022.108913, 2022.

Zhao, L., Zou, D., Hu, G., Du, E., Pang, Q., Xiao, Y., Li, R., Sheng, Y., Wu, X., Sun, Z., Wang, L., Wang, C., Ma, L., Zhou, H., and Liu, S.: Changing climate and the permafrost environment on the Qinghai–Tibet (Xizang) plateau, Permafr. Periglac. Process., 31, 396–405, https://doi.org/10.1002/ppp.2056, 2020.

Zhao, L., Zou, D., Hu, G., Wu, T., Du, E., Liu, G., Xiao, Y., Li, R., Pang, Q., Qiao, Y., Wu, X., Sun, Z., Xing, Z., Sheng, Y.,

https://doi.org/10.5194/egusphere-2026-5035
Preprint. Discussion started: 18 September 2026

Zhao, Y., Shi, J., Xie, C., Wang, L., Wang, C., and Cheng, G.: A synthesis dataset of permafrost thermal state for the Qinghai–Tibet (Xizang) Plateau, China, Earth Syst. Sci. Data, 13, 4207–4218, https://doi.org/10.5194/essd-13-4207-2021, 2021.

Zhao, L., Hu, G., Liu, G., Zou, D., Wang, Y., Xiao, Y., Du, E., Wang, C., Xing, Z., Sun, Z., Zhao, Y., Liu, S., Zhang, Y., Wang, L., Zhou, H., and Zhao, J.: Investigation, monitoring, and simulation of permafrost on the Qinghai-Tibet Plateau: A review, Permafr. Periglac. Process., 35, 412–422, https://doi.org/10.1002/ppp.2227, 2024.

Zhu, H., Zhang, X., Wei, G., Wang, Q., Liu, X., Yan, L., and Wang, G.: A method for better mapping of susceptibility to thaw hazards in data-scarce cold regions, Remote Sens. Environ., 337, 115338, https://doi.org/10.1016/j.rse.2026.115338, 2026a.

Zhu, H., Zhang, X., Wei, G., Wang, Q., Wang, G., and Liu, X.: Climate-driven thaw slump susceptibility on the Qinghai–Tibet Plateau using geographically explainable machine learning, Geosci. Front., 102384, https://doi.org/10.1016/j.gsf.2026.102384, 2026b.

Zhu, Y., Yin, K., Yang, H., Zhou, C., Wang, Z., and Liao, Y.: Temporal validity of landslide inventories in hazard mapping: insights from Hubei Province, China, Landslides, 23, 417–432, https://doi.org/10.1007/s10346-025-02651-3, 2026c.

Zou, D., Pang, Q., Zhao, L., Wang, L., Hu, G., Du, E., Liu, G., Liu, S., and Liu, Y.: Estimation of permafrost ground ice to 10 m depth on the Qinghai-Tibet Plateau, Permafr. Periglac. Process., 35, 423–434, https://doi.org/10.1002/ppp.2226, 2024a.

Zou, D., Pang, Q., Zhao, L., Wang, L., Hu, G., Du, E., Liu, G., Liu, S., and Liu, Y.: Permafrost ground-ice content to 10 m depth on the Qinghai-Tibet Plateau, National Tibetan Plateau Data Center [data set], https://doi.org/10.11888/Cryos.tpdc.300748, 2024b.